New Insights Into the Reservoir Landslide Deformation Mechanism From InSAR and Numerical Simulation Technology

Guoshi Liu , Bin Wang , Qian Sun , Jun Hu , *Senior Member, IEEE*, Lei-Lei Liu, Wanji Zheng , and Liye Zou

Abstract—Reservoir landslides represent a significant geological hazard that jeopardizes the safety of reservoirs. Deformation monitoring and numerical simulation are essential methodologies for elucidating the evolutionary patterns of landslides. Nonetheless, the existing approaches exhibit limitations in revealing the potential deformation mechanism. Consequently, this study proposes an innovative strategy that incorporates interferometric synthetic aperture radar (InSAR) deformation characteristics alongside fluid–solid coupling stress analysis to investigate the deformation, focusing on the Shuizhuyuan landslide within the Three Gorges Reservoir area as a case study. Using temporary coherence point InSAR technology, significant motion units were identified, with a maximum deformation rate of -60 mm/yr. The complete deformation time series reveals three independent components of landslide movement and their trigger factors geometrically. Subsequently, the saturation permeability coefficient of the sliding mass in the seepage analysis is modified with the assistance of InSAR deformation. Then, we coupled the seepage analysis results to FLAC3D model for stress and strain analysis, and determined the seepage-induced progressive failure mechanism and the deformation mode of the Shuizhuyuan landslide, driven by reservoir water-level (RWL) drop. The numerical simulation results aid in interpreting the deformation mechanism of different spatial and temporal patterns of landslides from three aspects: hydrodynamic pressure from rainfall infiltration, groundwater hysteresis caused by RWL drop, and seepage forces from RWL rise. Furthermore, our findings reveal that the dynamic factor of safety (FOS) of landslide during the InSAR observation period is highly consistent with the periodic fluctuations of the RWL. However, there is also a small trend of overall decline in FOS that cannot be ignored.

Index Terms—Deformation mechanism, fluid–solid coupling analysis, independent component analysis (ICA), interferometric synthetic aperture radar (InSAR), numerical simulation, Shuizhuyuan landslide.

I. INTRODUCTION

THE construction of large reservoirs has brought significant social and economic benefits in flood control, power generation, shipping, irrigation, and tourism. However, the impoundment of reservoirs can induce strain softening of rock and soil along the banks, leading to the occurrence of new landslides and the reactivation of ancient ones [1], [2]. In China, reservoir landslides are prevalent in the reservoir areas of several world-class hydropower projects, including Wudongde [3], Pubugou [4], Laxiwa [5], and Baihetan [6], among others. The stability of these landslides is highly sensitive to reservoir water-level fluctuation (FRWL) and rainfall, which can trigger geological hazards, such as swell [7] and barrier lakes [1], posing significant risks to the safety of reservoir. Consequently, reservoir landslides have garnered special attention from researchers.

Surface deformation is the direct manifestation of mass movement of reservoir landslides, which is influenced by both internal and external factors, such as rainfall, FRWL, and geological structure [8], [9]. Deformation monitoring has been widely utilized by researchers to understand the spatiotemporal evolution characteristics of landslide movement for the purpose of landslide prevention and warning [10]. Although global navigation satellite system (GNSS) technology is a conventional monitoring method with high precision [2], [4], it faces limitations in describing the spatial pattern of deformation for reservoir landslides due to sparse monitoring points. In recent decades, interferometric synthetic aperture radar (InSAR) technology has emerged as a crucial tool for the early identification and deformation monitoring of reservoir landslide, offering advantages, such as high spatiotemporal resolution and the capability to track historical deformation [3], [6], [11], [12], [13], [14], [15]. Moreover, the extensive monitoring points generated by InSAR technology provide a rich dataset for analyzing the correlation between deformation signals and triggering factors. Many researchers have utilized cross-correlation analysis of deformation

Guoshi Liu is with the School of Geosciences and Info-Physics, Central South University, Changsha 410083, China, and also with the School of Civil Architectural Engineering, Shaoyang University, Shaoyang 422000, China (e-mail: guoshiliu@csu.edu.cn).

Bin Wang is with the Key Laboratory of Natural Resources Monitoring in Tropical and Subtropical Area of South China, Ministry of Natural Resources, Guangzhou 510663, China (e-mail: gd_wbremote0919@foxmail.com).

Qian Sun is with the College of Geographic Science, Hunan Normal University, Changsha 410081, China (e-mail: sandra@hunnu.edu.cn).

Jun Hu, Lei-Lei Liu, and Wanji Zheng are with the School of Geosciences and Info-Physics, Central South University, Changsha 410083, China (e-mail: csuhujun@csu.edu.cn; csulll@foxmail.com; zhengwanji@csu.edu.cn).

Liye Zou is with the School of Civil Architectural Engineering, Shaoyang University, Shaoyang 422000, China (e-mail: 3684@hnsyu.edu.cn).

Digital Object Identifier 10.1109/JSTARS.2024.3523294

response characteristics to investigate the triggering mechanisms of reservoir landslides [5], [16], facilitating a discussion on the deformation evolution of complex landslides. It is important to recognize that InSAR results primarily offer a geometric interpretation of the deformation response and may struggle to elucidate the stress–strain relationship between deformation and triggering factors or reveal the characteristics of potential slide planes. In addition, it is challenging to assess the risk of landslide instability based on a unified deformation threshold due to significant differences in deformation scales among different landslides. However, this risk assessment is essential to assist the prevention and early warning of landslide disasters [4], [17].

Different from monitoring surface displacement, numerical simulation, which is based on the constitutive model of rock and soil materials combined with internal and external dynamics boundary conditions, is used to quantitatively analyze the seepage field, stress–strain field, and factor of safety (FOS) of reservoir landslide [8]. Generally, changes in groundwater conditions are the primary drivers of deformation or instability in reservoir landslides. Several scholars have proposed practical empirical formulae to fit soil–water characteristic curves (SWCCs) and hydraulic conductivity functions (HCFs) [18], [19], which are helpful for analyzing seepage in unsaturated soil within reservoir landslides. In addition, based on the principle of effective stress, Fredlund and Rahardjo [20] derived a constitutive equation for unsaturated soil medium, which can be used to quantitatively determine the stress state under coupled dynamic seepage conditions in reservoir landslides. Furthermore, the stability of reservoir landslides can be evaluated by considering the relationship between antisliding force and sliding force on the sliding body [17], [21]. The strength reduction method can utilize the stress state to simulate and calculate the potential slide plane shape and failure deformation mode [22]. These studies highlight the numerical simulation method as a crucial tool for uncovering the deformation mechanism, instability risk, and failure mode of reservoir landslides [8]. However, researchers often focus on specific sections due to the complexity of 3-D geological structure [4], [17], [21], which is insufficient for analyzing the spatial characteristics of landslide deformation. Moreover, the accuracy of the saturation permeability coefficient in reservoir landslides significantly influences the reliability of numerical simulation results. Given the spatial heterogeneity and perturbations in sample data, accurately measuring saturation permeability remains a significant challenge.

Currently, numerous scholars have conducted research on typical reservoir landslides utilizing InSAR or numerical simulation technology. However, both methods have certain limitations when independently studying reservoir landslides. The open-access strategy of Sentinel-1A significantly lowers the barriers to acquiring SAR images, enabling the rapid extraction of the spatial and temporal characteristics of reservoir landslide deformation. In addition, the 1-D pore water diffusion model can be employed to modify the permeability coefficient of rock and soil materials [5], [12], [23], thereby enhancing the accuracy of numerical simulation results for reservoir landslides. This article proposes an innovative strategy to investigate the deformation mechanism of reservoir landslides by considering InSAR deformation characteristics and fluid–solid coupling analysis. Initially, the multitemporal InSAR (MT-InSAR) technique is employed to reconstruct the deformation field of reservoir landslides, while the independent component analysis (ICA) method is used to analyze trigger factors related to the independent components of deformation. Second, the saturation permeability coefficient of the sliding body is modified based on the InSAR deformation time series. Subsequently, the seepage analysis results were coupled to the FLAC3D model for stress–strain analysis. Finally, we investigate the deformation mechanisms of reservoir landslides by integrating insights from InSAR deformation spatiotemporal patterns with results from fluid–solid coupling analysis. The Three Gorges Reservoir (TGR) is a high-risk area with numerous landslide disasters and has become a research hotspot in reservoir landslide. Since the impoundment of the TGR in 2003, nearly 5000 wading landslides have been identified [24], and 8 landslide disasters have occurred [25]. The Shuizhuyuan is a megalandslide in the TGR area and has been reactivated by the reservoir's impoundment. In recent years, significant signs of deformation have been observed [26], posing a potential threat to shipping on the Yangtze River. However, its deformation mechanism and stability remain unclear. Therefore, this study incorporates InSAR and numerical simulation technology into the safety program of the Shuizhuyuan landslide, employing our proposed strategy to investigate its deformation.

II. STUDY AREA AND DATASETS

A. Geological Background of Shuizhuyuan Landslide

The Shuizhuyuan landslide is one of the megalandslide within the TGR area. It is situated on the north bank of the Yangtze River in Quchi Township, Wushan County, Chongqing City, China, approximately 170 km upstream from the Three Gorges Dam [26], as depicted in Fig. 1(a). The trailing edge of the landslide is at an elevation of 350 m, while the slope toe is at 90 m [see Fig. 2(b)]. The main sliding direction is estimated at N147°, with the landslide extending approximately 800 m in length and varying in width from 360 to 1200 m. The average thickness is about 30 m, covering an area of approximately 62×10^4 m^2, and the total volume is about 1850×10^4 m^3 [26]. The stability of the Shuizhuyuan landslide has been adversely affected by the strain softening of the slope toe due to the impoundment of the TGR [2] and the bank erosion caused by periodic FRWL [27]. The macroscopic deformation investigations reveal the presence of cracks at the trailing edge, residential buildings, and the front edge of the landslide, as shown in Fig. 1(c)–(e). Furthermore, the Gongjiafang and Hongyanzi landslides, located 20 km downstream from Shuizhuyuan, have experienced failure disasters, with these medium-sized landslides resulting in a swell of over 20 m [7]. Given the similar geological structure and seepage conditions, the Shuizhuyuan landslide's failure has the potential to lead to even more severe disasters. In recent years, significant deformation trends have been observed in the Shuizhuyuan landslide using GNSS. However, according to our statistics, there are only three studies pertaining to this landslide, which focus on the
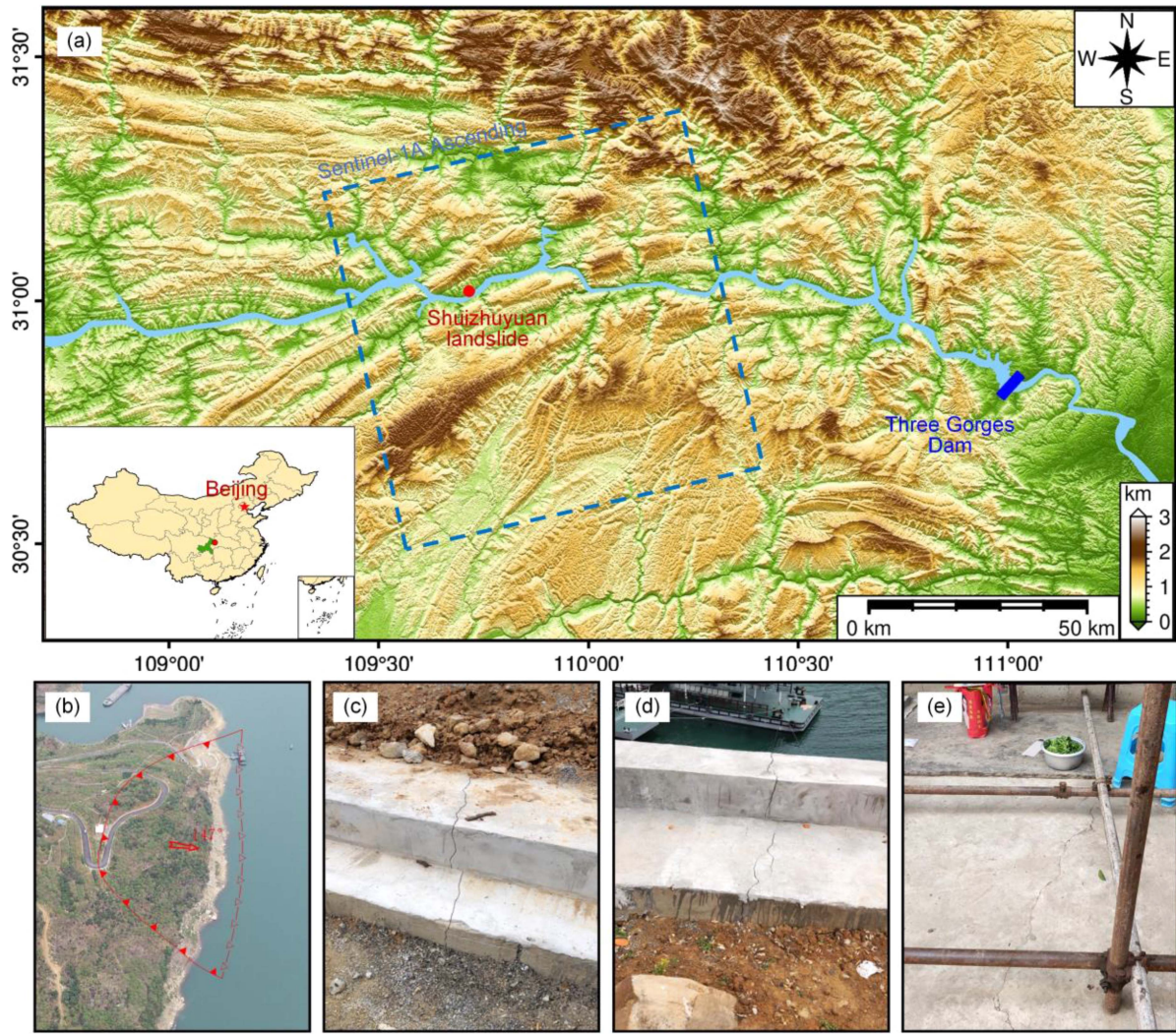
Fig. 1.   Location of the study area. (a) DEM image of the TGR. The inset shows the location of the landslide in China. (b) UAV image of the landslide. (c)–(e) Surface deformation signs of the landslide.

GNSS displacement prediction based on the machine learning methods [26], [28], [29]. The sparse distribution of GNSS monitoring points inadequately captures the temporal and spatial evolution of deformation. In addition, the potential failure modes, deformation mechanisms, and dynamic response characteristics of the FOS for the Shuizhuyuan landslide remain unclear. Consequently, it is imperative to conduct InSAR monitoring and numerical simulation analysis for the Shuizhuyuan landslide.

No obvious regional fault was found near the Shuizhuyuan landslide. The detailed stratigraphic situation is shown in Fig. 2(c). The exposed strata in the study area are Triassic, Jurassic, and Quaternary, in chronological order from oldest to youngest. The main strata are Triassic $T_{1-2}j$ and Middle Triassic Series (T_2b). According to the field investigation, the Shuizhuyuan landslide is an accumulative landslide, with its sliding mass mainly consisting of accumulated deposit (Q_4^{del}) and colluvial deposit (Q_4^{col}). The accumulated deposit (Q_4^{del}) comprises a mixture of gravel and silty clay [see Fig. 2(b)]. Due to its large pore space, this layer facilitates surface water infiltration and functions as an active seasonal aquifer, adversely

affecting slope stability [16]. The bedrock at the front and back of the landslide is composed of marl (T_2b) from the Middle Triassic series, while the bedrock in the middle belongs to the Upper Triassic Series (T_3j).

B. Datasets

The experiment acquired 196 Sentinel-1A ascending images from January 2017 to December 2023, with a maximum time interval of 60 days. These SAR images were utilized to identify the temporal and spatial deformation characteristics of the Shuizhuyuan landslide. In addition, the 30-m resolution shuttle radar topography mission digital elevation model (SRTM DEM) was employed for geocoding and topographic phase removal. The parameters of the Sentinel-1A dataset used in this study are presented in Table I.

In general, FRWL and rainfall are the primary triggering factors for landslide deformation and failure in the TGR area [2], [16], [17]. Relevant authorities have released real-time reservoir water level (RWL). In addition, the Wushan meteorological
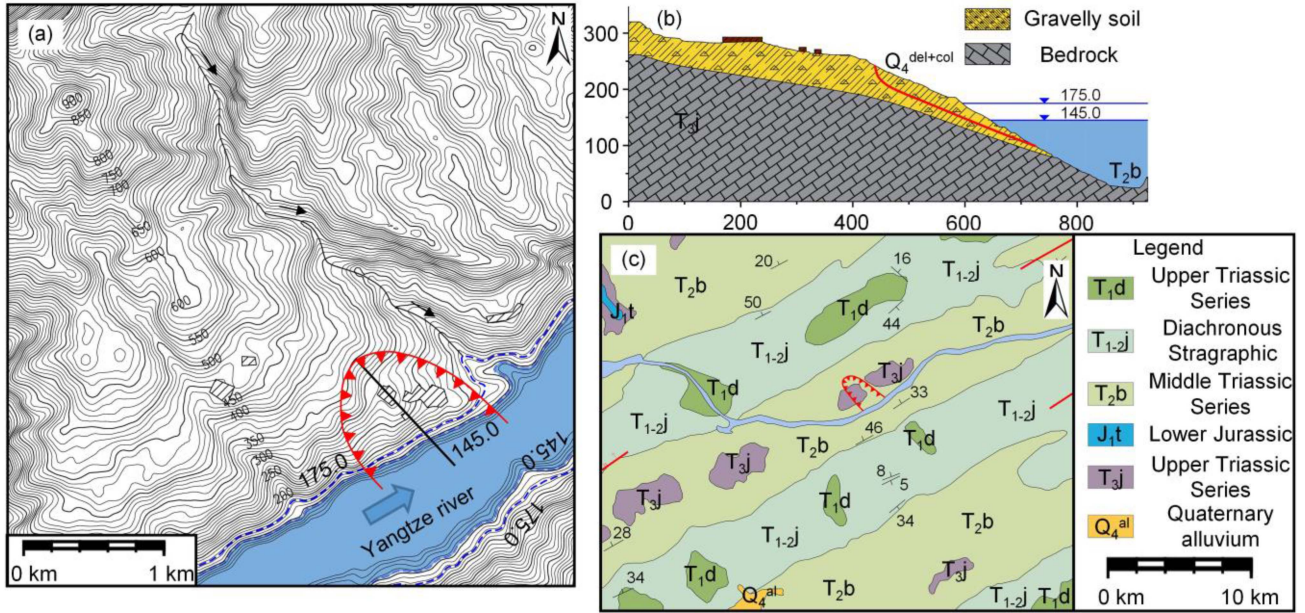
Fig. 2. Landslide geological conditions. (a) Engineering geological plane, the black thick line is the main sliding surface. (b) Engineering geological profile, the red line is the presumed sliding surface. (c) Lithologic map with a scale of 1:250 000 showing the geological setting of the surrounding areas.

<table>
<tr><td colspan="2" align="center">TABLE I
SAR DATA PARAMETERS</td></tr>
</table>

Category	Parameters
Orbit number	84
Orbit direction	Ascending
Heading angle (°)	347.3
Look angle (°)	39.3
Pixel spacing (m; Range × Azimuth)	2.3×13.9
Timespan	01/04/2017−12/23/2023
Number of scenes	196

TABLE II
GEOTECHNICAL MATERIAL PARAMETER

Material	Sliding mass	Bedrock
Saturated water	0.4	/
Residual water rate	0.15	/
Permeability coefficient (m/d)	0.01−0.3	0.001
Dry density (g/cm³)	1.6	2.22
Elastic modulus (Mpa)	200	1120
Poisson's ratio	0.25	0.22
Cohesive force (Kpa)	60	3380
Friction angle (°)	34	46

station, situated 17 km from the Shuizhuyuan landslide, records local rainfall at daily intervals. We collected these two hydrological datasets from 1 January 2016 to 1 May 2024 to aid in interpreting the deformation mechanisms of the landslide.

Relevant institutions have conducted a detailed investigation of potential geological disaster sites in the TGR area, with a particular focus on the Shuizhuyuan landslide. The material parameters used in the numerical simulation for this study are primarily based on the investigation report of Shuizhuyuan landslide, including seepage and strength parameters. In addition, some parameters are referenced from previous studies of similar landslides in the TGR area. Detailed geotechnical parameters are provided in Table II.

III. METHODS AND DATA PROCESSING

A. Temporal and Spatial Pattern of InSAR Deformation

1) Temporary Coherence Point InSAR (TCP-InSAR): The temporary coherence point (TCP) of the small baseline subset (as shown in Fig. 3) is utilized as observations to balance both the number and coherence of point targets during MT-InSAR
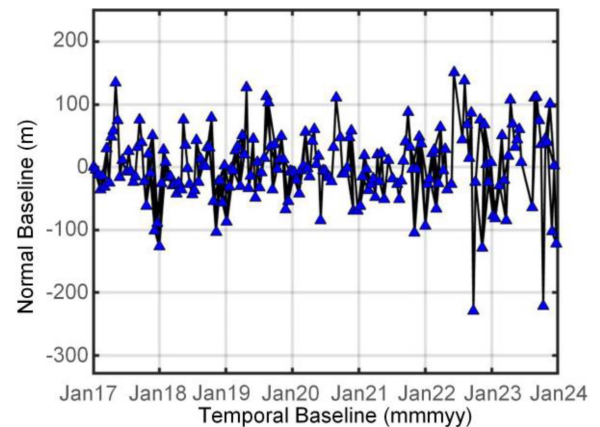

Fig. 3. InSAR image pairs.

processing [see Fig. 4(a)] [30], [31]. It is assumed that i interferograms are selected from j SAR images in the study period. The deformation rate of the TCP on the ith interferogram is v, and the deformation phase relative to the main image can be expressed
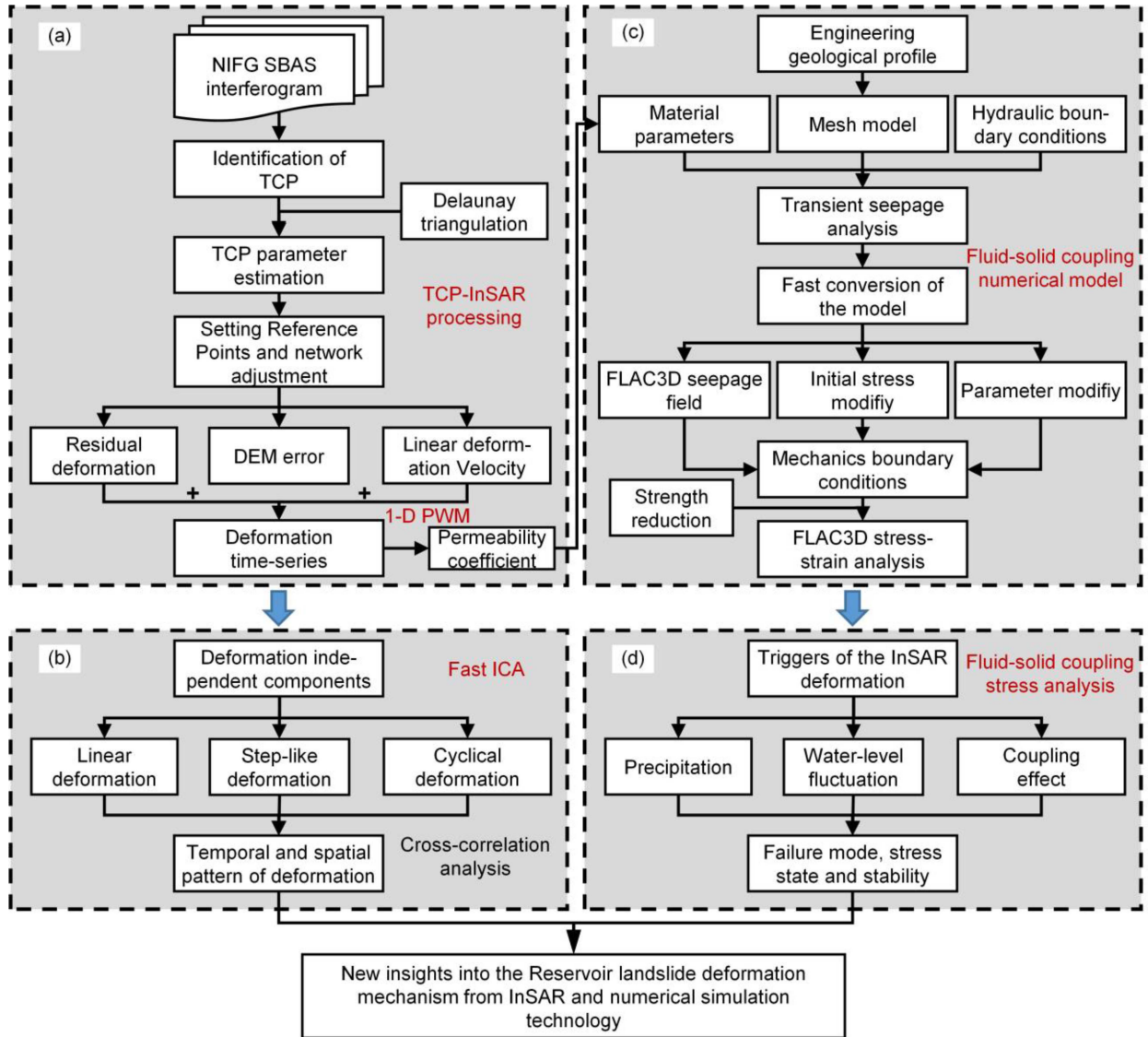
Fig. 4.   Flowchart of this study. (a) TCP-InSAR processing. 1-D PWM represents the 1-D pore water diffusion model. (b) Spatiotemporal pattern of InSAR deformation. (c) Fluid–solid coupling numerical model. (d) Stress analysis.

as follows:

$$\emptyset_{\text{def},l,m}^{i}= -\frac{4\pi}{\lambda}\Delta\, r_{l,m}^{i} = \sum_{k=1}^{C_i-1}(t_k - t_{k-1})\, v_k = \beta_i\, v \quad (1)$$

where (l, m) is the pixel coordinate of the TCP, $r_{l,m}^{i}$ is the distance between the ground coordinates and the sensor, λ is the radar wavelength, and t is the time. The topographic residual phase $\emptyset_{\text{topo},l,m}^{i}$ is positively correlated with the spatial baseline $B_{\perp}^{i}$ of the image pair, which can be expressed as follows:

$$\emptyset_{\text{topo},l,m}^{i}= -\frac{4\pi}{\lambda}\frac{B_{\perp}^{i}}{r_{l,m}^{i}\sin\theta^{i}}\Delta\, h_{l,m} = \alpha_{l,m}^{i}\,\Delta h_{l,m} \quad (2)$$

here θ^{i} is the local incidence angle. To overcome the influence of unwrapping error, the TCP-InSAR method takes the phase

difference between adjacent TCPs as the observation

$$\Delta\emptyset_{l,m,l',m'}^{i}=\alpha_{l,m}^{i}\,\Delta h_{l,m,l',m'} + \beta_i\Delta v + w_{l,m,l',m'}^{i}. \quad (3)$$

Since the atmospheric delay exhibits strong spatial correlation, Li et al. [32] confirmed that the atmospheric delay between adjacent points can be disregarded through the phase difference of the arc. The random noise $w_{l,m,l',m'}^{i}$ after the phase difference satisfies statistical characteristics with a mathematical expectation of 0. For short arcs without phase ambiguity, the time series can be expressed as follows:

$$\Delta\emptyset = [\alpha\ \beta]\begin{bmatrix}\Delta h_{l,m,l',m'}\\ \Delta v\end{bmatrix} + w \quad (4)$$

where $\Delta\emptyset = [\Delta\emptyset_{l,m,l',m'}^{1}\ \Delta\emptyset_{l,m,l',m'}^{2}\ \cdots\ \Delta\emptyset_{l,m,l',m'}^{i}]$, $\alpha = [\alpha_{l,m}^{1}\ \alpha_{l,m}^{2}\ \cdots\ \alpha_{l,m}^{i}]^{T}$, and $\beta = [\beta_1\ \beta_2\ \beta_i]^{T}$ are the coefficient

matrices of deformation rates and DEM errors, respectively. The parameters in (4) can be solved using the least squares method. To enhance the reliability of the solution, proper phase thresholds are set to select valid arcs. The selected arcs are then reconstructed into a Delaunay triangulation network for quadratic estimation of the parameters. Finally, integrating the results of parameter estimation with reference points allows for the generation of deformation rates and DEM errors for each TCP.

2) Estimation of Trigger Factors and Lag Time by ICA: Supposing that a set of InSAR observations $X_1(t), X_2(t), \ldots, X_n(t)$ is generated by the linear combination of independent components, which can be expressed as follows:

$$[X_1(t), X_2(t), \ldots, X_n(t)]^T$$
$$= A \cdot [S_1(t), S_2(t), \ldots, S_n(t)]^T \quad (5)$$

where the coefficient matrix A represents the linear combination of different components, and $S(t)$ represents the independent component of the deformation. ICA can decompose InSAR deformations into multiple components with different spatial scores and time characteristics based on the independence assumption [33]. The independent components generated by ICA can be regarded as the spatiotemporal patterns of deformation caused by different triggers.

Due to the varying coupling mechanisms between triggering factors and deformation, the movement characteristics of reservoir landslides can exhibit diverse forms, as seen in the Huangtupo landslide [34] and Xinpu landslide [16] in the TGR area. While the revisit period of Sentinel-1A in the TGR region is at least 12 days, the sampling interval for rainfall and RWL data is 1 day. To ensure consistency, rainfall and RWL data were resampled to match the temporal frequency of Sentinel-1A for normalized cross-correlation analysis with the deformation-independent component [33]. To account for potential time lags, a one-day sliding window was employed to quantify the impact of the trigger factors [16]. The time step with the highest correlation was ultimately identified as the lag time of the trigger factors.

3) Modification of Seepage Parameters Based on InSAR: In seepage analysis, accurately estimating the permeability coefficient is crucial. However, the permeability coefficient obtained from tests is often presented as a range, with differences in magnitude reaching up to 1.0e-2. The 1-D pore water diffusion model can invert the hydraulic diffusion coefficient using InSAR time-series deformation and rainfall records [5], [12]. This model is employed in this article to depict the change in transient pore water pressure caused by rainfall infiltration

$$\frac{dP}{dt} = D\frac{d^2P}{dz^2} \quad t > 0, z > 0 \quad (6)$$

where P is the pore water pressure, D is the hydraulic diffusion coefficient, and z is the depth. This model describes the propagation process of pore water pressure in landslide. Rainfall record $R(t)$ and scale factor q are used to describe the surface pore water pressure

$$P(t, z = 0) = q.R(t). \quad (7)$$

The analytical solution of this propagation process has been given as follows [5]:

$$P(t, z) = \frac{z}{2\sqrt{\pi D}} \int_0^t \frac{e^{-\frac{z^2}{4D(t-s)}}}{\sqrt{(t-s)^3}} P(s, z = 0)\, ds \quad (8)$$

where s is the time variable. Iverson related the hydraulic diffusion coefficient to the permeability coefficient [23]

$$D = \frac{k}{C}, \ D_0 = \frac{k_s}{C_0} \quad (9)$$

where C represents the measurement of volumetric water content with pore water pressure, which reaches the minimum value C_0 when the soil is saturated. Accordingly, the hydraulic diffusion coefficient will reach the peak value D_0, and k_s represents the saturation permeability coefficient.

B. Fluid–Solid Coupling Analysis

In this study, a numerical model with fluid–solid coupling analysis will be established to investigate the deformation mechanism, failure mode, and dynamic response characteristics of the FOS of landslide. The technical process is illustrated in Fig. 4(c). To balance the geometric size of the landslide [see Fig. 2(b)] with computational efficiency, we set the grid spacing to 8 m for the sliding mass and 15 m for the bedrock. The model consists of 1514 grids and 1438 zones, as shown in Fig. 5.

1) Unsaturated Seepage Analysis: In the seepage field, the 2-D seepage differential equation is used to describe the change of the volume water content of the grid in a certain time

$$\frac{\partial}{\partial x}\left(k_x \frac{\partial H}{\partial x}\right) + \frac{\partial}{\partial y}\left(k_y \frac{\partial H}{\partial y}\right) + Q = \frac{\partial \theta}{\partial t} \quad (10)$$

where H is the hydraulic head, k_x and k_y represent the permeability coefficients in the *x* and *y* directions, respectively, Q is the applied boundary flow, and θ is the volume water content. In reservoir landslide, rainfall and FRWL will cause the change of saturation of rock and soil, which shows its unsaturated character. For seepage analysis in unsaturated soils, we estimate SWCC based on the moisture content of the material sample function in the GeoStudio SEEP/W module. HCF is estimated by Van Genuchten [19] method based on SWCC, as shown in Fig. 6.

Hydraulic boundary conditions are crucial for accurately solving the seepage field. The seepage boundary conditions applied in this study are depicted in Fig. 5(a) and are as follows.

1) The left boundary was set with a fixed hydraulic head of 230 m.
2) The unit flow boundary condition, with a magnitude equal to the intensity of rainfall, was applied to the landslide slope.
3) The hydraulic head and drainage conditions were set on the reservoir slope, with the height corresponding to the RWL.
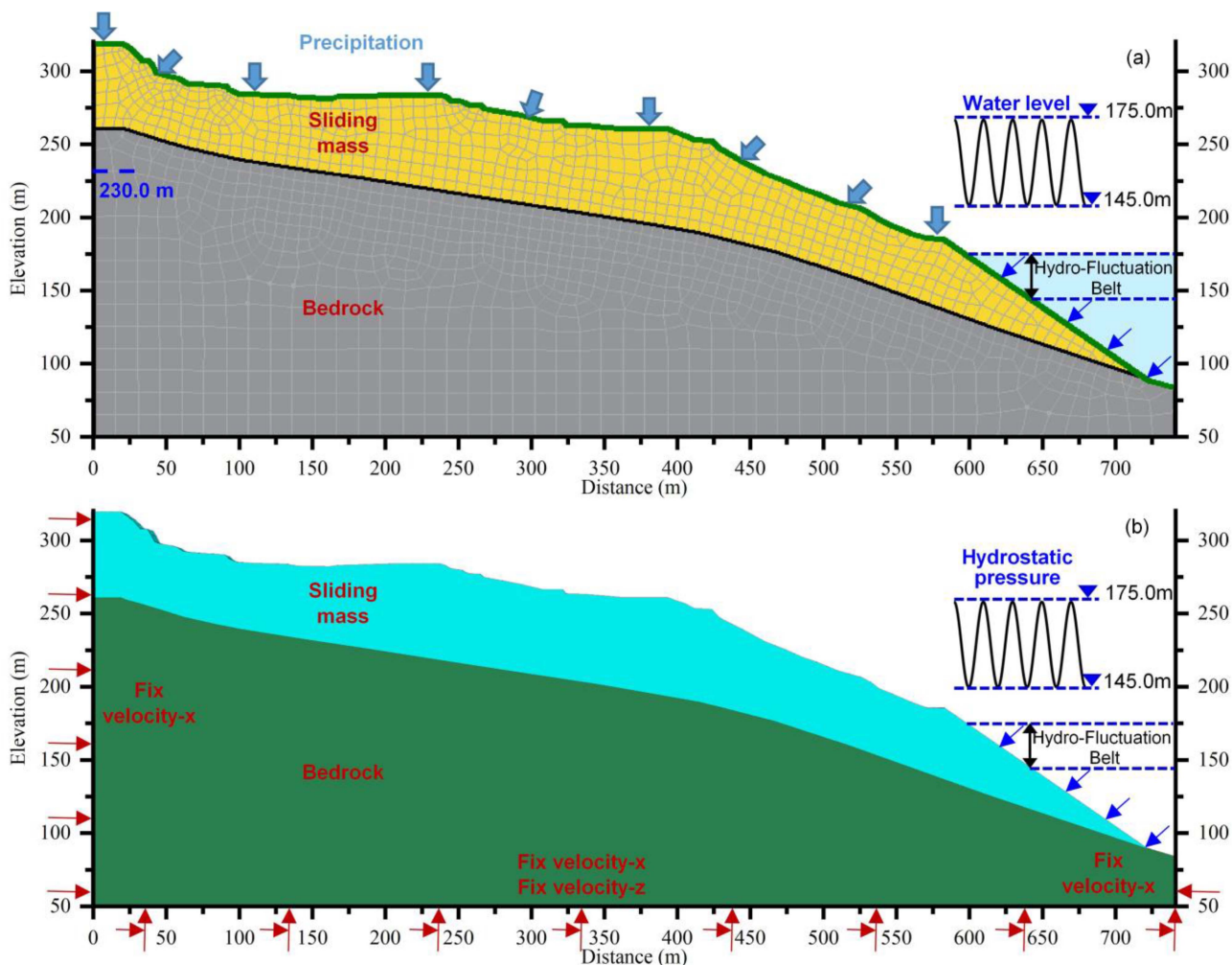4) Impervious conditions were applied to all other outer boundaries.

Fig. 5. Numerical model and boundary conditions of the Shuizhuyuan landslide. (a) Seepage analysis. (b) Stress–strain analysis.
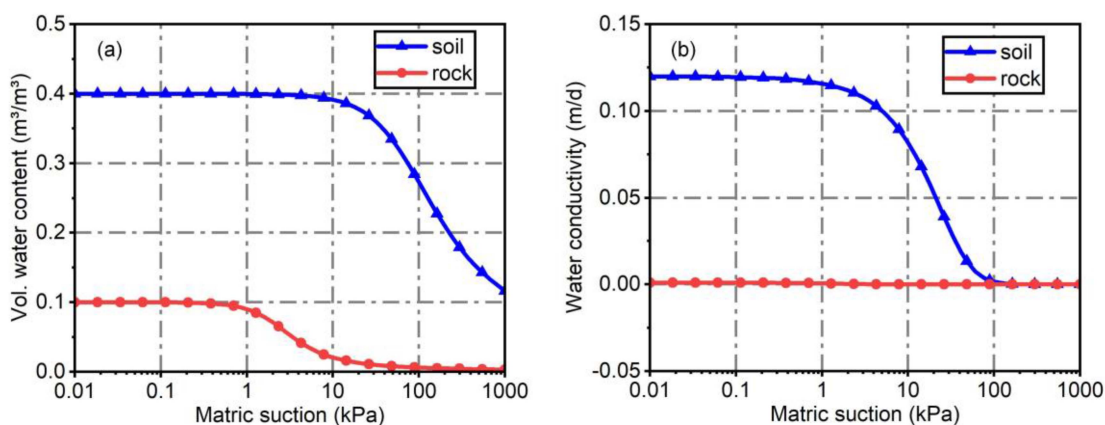

Fig. 6. Unsaturated characteristics of the Shuizhuyuan landslide. (a) SWCC. (b) HCF.

The external dynamic factors influencing the stability of the Shuizhuyuan landslide are likely rainfall and FRWL. To reveal the potential mechanical mechanisms, we designed four seepage scenarios as hydraulic boundary conditions for the numerical simulations, as outlined in Table III. For numerical calculations, GeoStudio software, which is based on the finite-element method, offers robust functions for unsaturated seepage analysis and has become the mainstream commercial software for seepage analysis in geotechnical engineering research [17].

| Scenarios	Variables	Boundary condition parameters
Scenario 1	Effect of rainfall only considered	The RWL is set to 175.0 m
		Measured daily rainfall from 01-11-2016 to 31-10-2017
Scenario 2	Reservoir water level changes only	The rainfall is set to 0.0 mm/d
		The water level decreased from 175.0 to 145.0 m at a rate of 0.2 m/d
		The water level rose from 145.0 to 175.0 m at a rate of 0.5 m/d
Scenario 3	Coupling effect	Measured daily rainfall from 01-11-2016 to 31-12-2023
		Measured RWL from 01-11-2016 to 31-12-2023
Scenario 4	Effect of reservoir water level rapidly decline only	The rainfall is set to 0.0 mm/d
		The rainfall is set to 0.0 mm/d
		The water-level decline rate is set to 0.5 m/d
		The water-level decline rate is set to 0.6 m/d
		The water-level decline rate is set to 1.0 m/d
		The water-level decline rate is set to 2.0 m/d
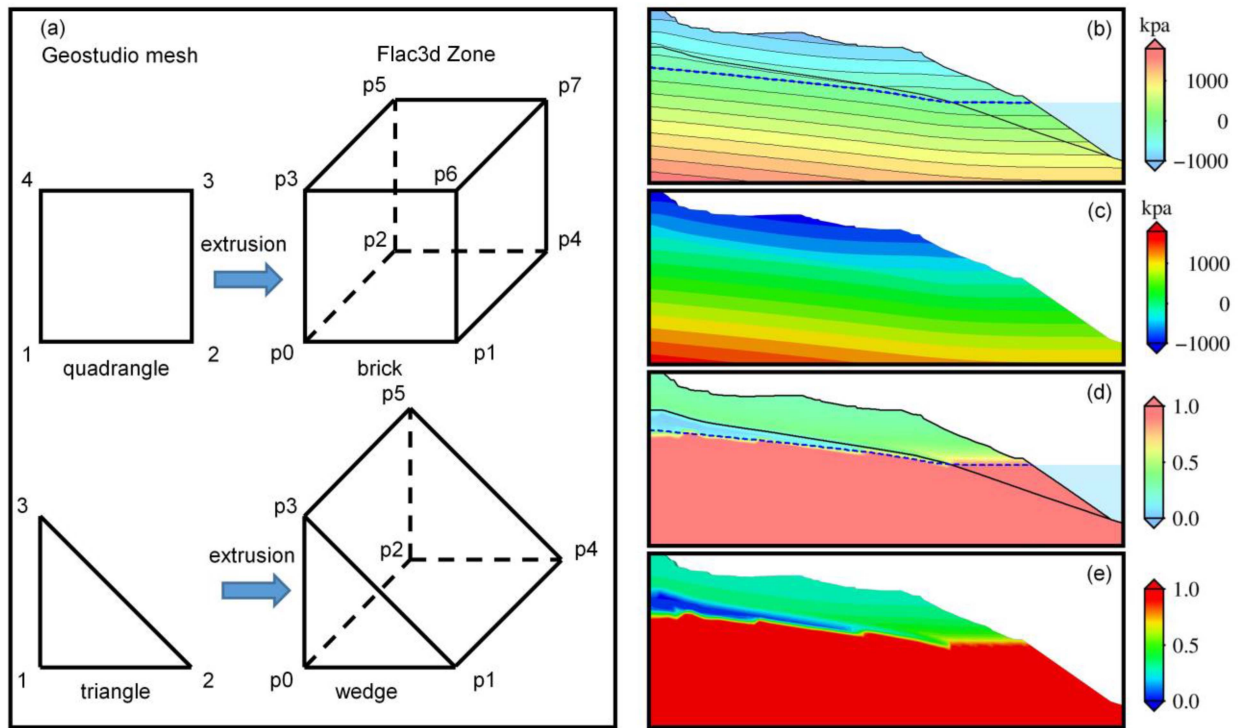
Fig. 7. Conversion of seepage field. (a) Correspondence between GeoStudio and FLAC3D grid. (b) Pore pressure (GeoStudio). (c) Pore pressure (FLAC3D). (d) Saturation (GeoStudio). (e) Saturation (FLAC3D).

2) Stress–Strain Analysis: According to the principle of effective stress, changes in seepage conditions inevitably influence the mechanical properties of soil. Consequently, many researchers conduct landslide stress analysis by coupling the seepage field. Among the available tools, GeoStudio offers various limit equilibrium methods frequently used to calculate the FOS of reservoir landslides [17], [21]. However, GeoStudio has limitations in simulating large deformations. FLAC3D, a software developed using the fast Lagrangian finite difference method, overcomes convergence issues related to large deformations. Nevertheless, it poses challenges when handling complex

hydraulic boundary conditions for unsaturated seepage analysis. Hence, this study couples the seepage field calculated by GeoStudio with a FLAC3D model for stress and strain analysis, as depicted in Fig. 4(c). This process consists of three main steps.

1) Model conversion of seepage field.

   The normal stretching of GeoStudio's 2-D mesh model transforms the triangular mesh into wedge and the quadrangle into brick, respectively. Fig. 7 illustrates the gride correspondence, pore pressure, and saturation of the model before and after stretching.

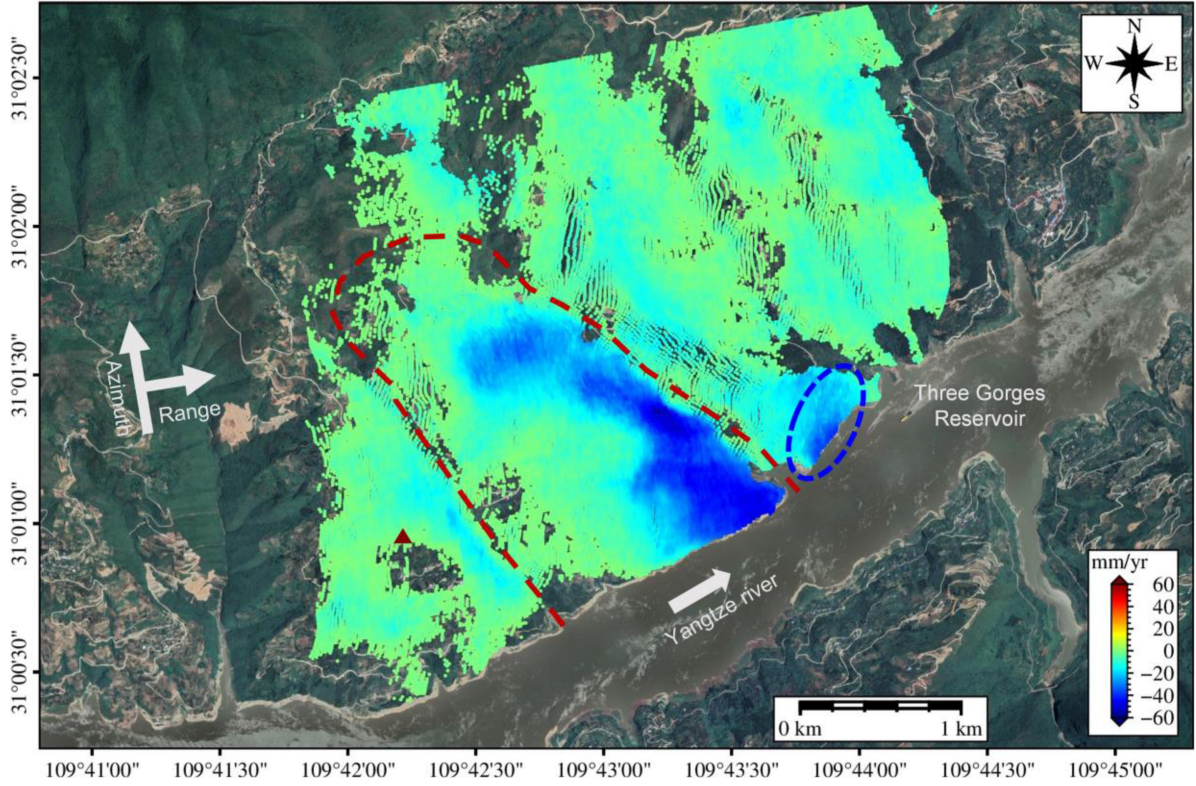2) Correction of initial stress.

Fig. 8.   LOS deformation rate maps of the Shuizhuyuan landslide. The red triangle represents the position of the reference point.

The introduction of pore pressure into the FLAC3D model alters the initial effective stress of soils, necessitating a correction to the initial total stress. Consequently, we adjust the initial total stress following the incorporation of pore pressure. In accordance with the principle of effective stress, the effective stress σ' of rock and soil can be represented as follows [35]:

$$\sigma' = \sigma - u_a - \sigma^s = \sigma - u_a - u_w \frac{S_r \theta_s - \theta_r}{\theta_s - \theta_r} \quad (11)$$

where σ is the total stress, u_a is the pore air pressure, the general value is 0; σ^s is the suction stress, which equals the pore pressure when the soil is saturated and equals the matrix suction when the soil is unsaturated, and S_r is the saturation. Assuming that the suction stress and total stress of the model are σ^s_0 and σ_0, respectively, before the pore pressure is introduced, and the suction stress after model import is σ^s_1, the modified initial total stress σ_1 can be expressed as follows:

$$\sigma_1 = \sigma_0 - \left(\sigma^s_0 - \sigma^s_1 \right). \quad (12)$$

3) Modification of model parameters.
    Assuming that ρ_d is the dry density of the material, the soil wet density ρ is corrected by porosity n and the density of water ρ_w

$$\rho = \rho_d + n S_r \rho_w. \quad (13)$$

Considering the transient saturated zone formed by rainfall infiltration, it is noted that the shear strength of rock and soil

will be reduced. For simplicity, the internal friction angles φ of the sliding mass are set to 33°, 32°, and 31° when the saturation exceeds 0.4, 0.6, and 0.8, respectively. When the saturation is less than 0.4, the internal friction angle is maintained at 34°. In unsaturated regions, pore pressure and friction angle are utilized to modify effective cohesive forces

$$C' = C + \text{abs}\left(u_w \right) \tan \varphi \quad (14)$$

where C is the cohesive force under saturation state.

The stress or displacement rate conditions, as shown in Fig. 5(b), are imposed to constrain the boundary of the model.
1) The normal displacement rate of the side is fixed.
2) The displacement rate in all directions at the bottom of the model is fixed.
3) The hydrostatic pressure boundary condition is set to simulate the counterpressure effect of the RWL on the reservoir slope.

IV. RESULTS AND ANALYSES

A. InSAR Deformation

In this study, 43 777 TCPs were identified to reconstruct the InSAR deformation fields of the Shuizhuyuan landslide, as shown in Fig. 8. Significant deformation was observed in the front and middle sections of the landslide during the monitoring period, with a maximum deformation rate of −60 mm/yr. In addition, movement units were detected at the trailing edge, exhibiting a maximum deformation rate of −40 mm/yr. It is
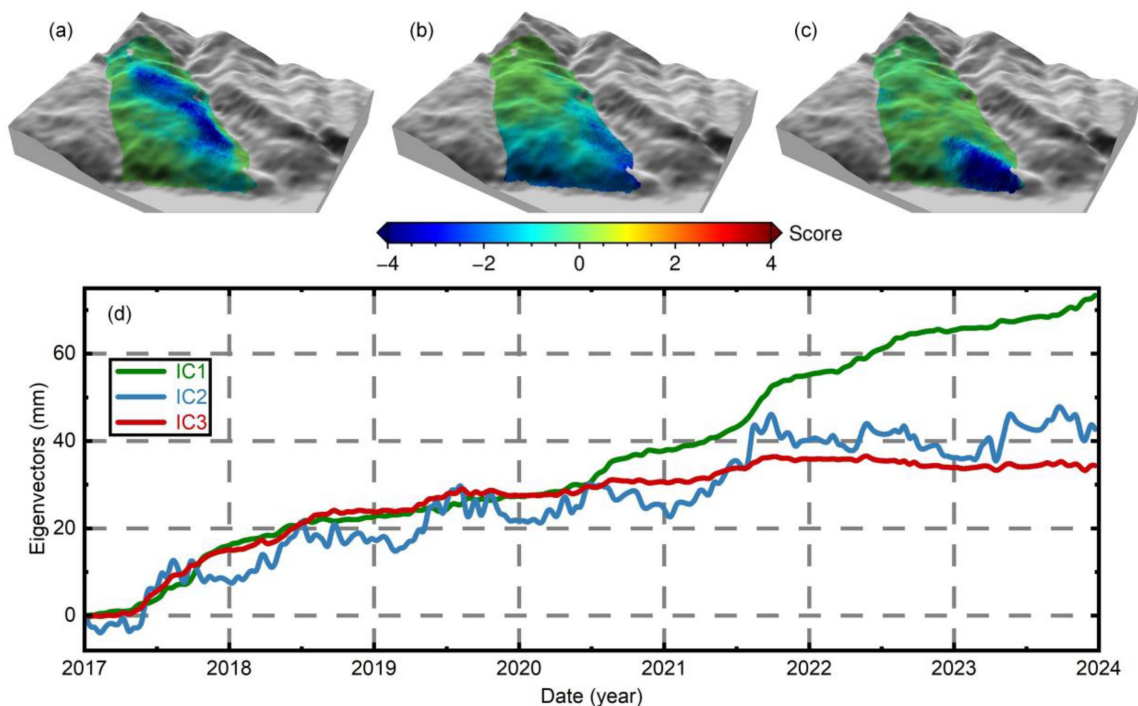
Fig. 9. ICA decomposition results for the InSAR time series. Contribution of (a) IC1, (b) IC2, and (c) IC3 derived by ICA. (d) Temporal eigenvectors of three independent components.

important to note that, due to the angle between the slope direction and the line-of-sight (LOS) direction being close to 60°, there may be reduced sensitivity in detecting deformations using InSAR, potentially leading to an underestimation of the actual deformation [12]. Therefore, a detailed study of the landslide deformation characteristics is crucial. Moreover, a significant movement unit was detected approximately 200 m downstream from the Shuizhuyuan landslide along the riverbank, displaying typical frontal-pulling characteristics and exhibiting a maximum deformation rate of −50 mm/yr (as indicated by the blue dashed line in Fig. 8).

The Shuizhuyuan landslide exhibits significant deformation in its frontal and central areas, although directly determining the specific mode of deformation (e.g., traction or push) from InSAR deformation rates alone is challenging. To address this, the study applies ICA to the InSAR deformation time series. This study focuses exclusively on the deformation of the Shuizhuyuan landslide. Deformation characteristics from other movement units could potentially interfere with the results of ICA for the study area [36]. With a view to highlighting the contribution of the independent components, we limited the ICA processing to the deformation area of interest within the landslide boundary, as indicated by the red dotted line in Fig. 8. The number of independent components can significantly influence the ICA results. Selecting too few components may lead to the cross fusion of distinct independent signals, resulting in the loss of detailed signal characteristics. Conversely, selecting too many components can dilute the signal strength of the principal components. In previous studies, the variance ratio of principal components is commonly employed as an empirical criterion for determining the optimal number of independent components

[36], [37]. Three distinct independent component signals (IC1, IC2, and IC3) were identified for the Shuizhuyuan landslide, with their cumulative variance ratio reaching 99.51%. Fig. 9 illustrates the spatial scores and temporal eigenvectors of the three independent components. It is important to note that the independent components in Fig. 9 do not indicate positive or negative contributions based on their sign of score values [36]. As shown in (5), the product of the spatial score and the eigenvector represent a deformation time series of the independent components. Given the overall trend of negative and continuously increasing deformation in the time series, the eigenvector was reversed to analyze the time–frequency relationship of triggering factors. This approach with the processing strategies employed in previous studies [16]. These components reveal different spatiotemporal patterns, suggesting diverse triggering mechanisms. IC1 predominantly affects the middle and trailing edges of the landslide, showing a continuous increase over time. In contrast, IC2 is mainly concentrated at the toe, with a spatial score inversely related to the distance from the reservoir. This component exhibits a relatively complex temporal pattern, characterized by an increasing trend and periodic fluctuations. Meanwhile, IC3 exhibits continuous growth over time similar to IC1 but is predominantly concentrated at the front position of the landslide and toe.

B. Triggers and Lag Time of the Shuizhuyuan Landslide in Different Sections

In order to comprehend the potential triggering factors of these three independent components, we compared them with precipitation and RWL. Fig. 10(a) shows the relationship among
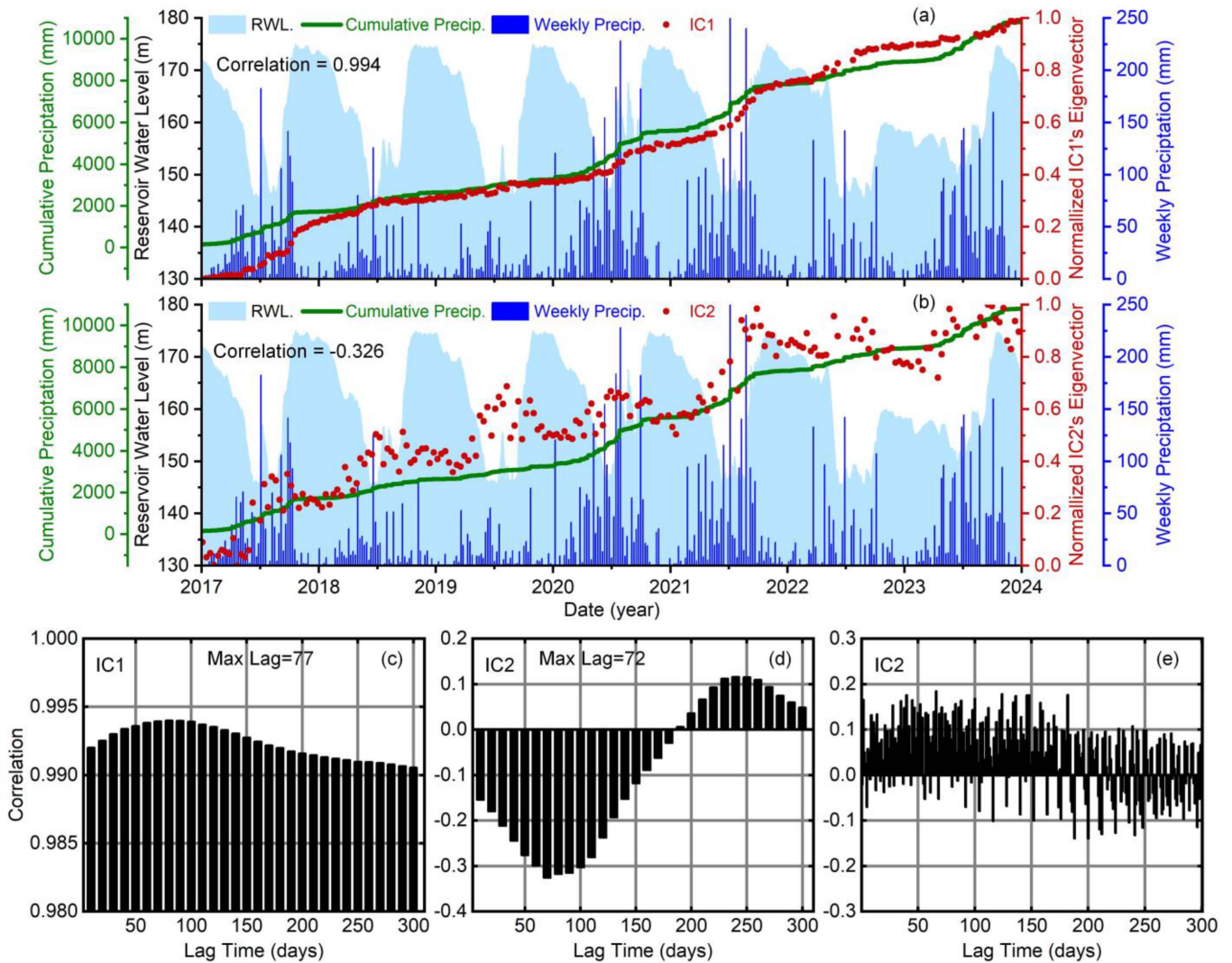
Fig. 10.   Cross-correlation estimation between the independent components of InSAR deformation and triggering factors. Comparisons among precipitation, water level, and normalized IC eigenvectors of (a) IC1 and (b) IC2. (c)–(e) Relationship between correlation and lag time for corresponding triggers.

the normalized eigenvector of IC1, precipitation, and RWL. IC1 exhibits distinct creep characteristics over time, with a relatively low correlation between this deformation and the periodic fluctuations in the RWL. Given the spatial characteristics of IC1, the FRWL is unlikely to be the direct cause of this deformation. Typically, continuous rainfall infiltration can trigger long-term creep behavior in slopes, with heavy rainfall events accelerating the deformation process [38]. In Fig. 10(a), weekly precipitation data are used to represent short-term rainfall behavior. From October to May of the following year, there was no significant heavy rainfall, and the IC1 time series showed a slow upward trend. However, in certain hydrological years (e.g., 2017, 2020, and 2021), heavy rainfall occurred from June to September, and the IC1 time series also exhibited an accelerated deformation trend during these periods, albeit with some time lag. Considering that the fluctuation signal of short-term rainfall will interfere with the cross-correlation coefficient of long-term creep behavior, we use long-term rainfall (cumulative precipitation) to perform cross-correlation analysis on IC1 [16], [33]. The results revealed

a strong correlation of 0.994 between long-term rainfall and IC1 deformation. Based on the spatial pattern [see Fig. 9(a)] and temporal evolution [see Fig. 10(a)] of IC1, it can be inferred that rainfall is the primary triggering factor for the deformation observed in the middle and trailing edge of the Shuizhuyuan landslide. This finding is consistent with the deformation scenarios of many landslides in the TGR area [16].

Generally, the evolution characteristics of the toe control the stability of reservoir landslide [16], [17]. Fig. 9 illustrates that both IC2 and IC3 make significant score to the deformation at the toe. We compare the normalized eigenvector of IC2 with RWL and precipitation. Fig. 10(b) shows that the time series of IC2 exhibits clear periodic behavior. When the RWL rises, the IC2 time series shows a downward trend, while it increases when the RWL declines. In addition, we observed that the deformation of IC2 appears to be related to precipitation. The deformation increases with higher short-term rainfall intensity and decreases when rainfall diminishes. Based on these observations, we performed cross-correlation analysis among RWL, daily precipitation, and

IC2. The results indicate a negative correlation between IC2 and the RWL [see Fig. 10(d)]. Due to the lower permeability coefficient of the landslide materials compared with the rate of FRWL, there is a noticeable delay in the deformation response of IC2 to these changes. Based on the spatial pattern of IC2, we infer that FRWL is the trigger for the periodic deformation of IC2. Periodic InSAR deformations at the toe induced by FRWL are common within TGR area, such as Muyubao landslide [39] and Xinpu landslide [16].

Unlike the FRWL, the cross-correlation analysis between IC2 and rainfall revealed no significant correlation [see Fig. 10(e)]. Given the discontinuous nature of short-term rainfall events, using daily precipitation to quantitatively assess the cross correlation with deformation components is not appropriate. Furthermore, the maximum correlation coefficient between FRWL and IC2 is only -0.326, suggesting that FRWL is not the sole factor driving IC2 deformation. In addition to periodic deformation, we also observed a continuous growth signal in IC2. As mentioned previously, continuous rainfall infiltration can trigger long-term creep behavior in slopes. This growth signal may be induced by prolonged rainfall, which is common in landslides in the TGR area [16], [40]. Therefore, we consider the combined effect of cumulative precipitation and FRWL to compare with IC2. Given the negative correlation between IC2 and RWL, we normalized the opposite of RWL and cumulative precipitation [see Fig. 11(a), cyan area]. The results show that this combined signal is more consistent with the eigenvector of IC2, with a correlation coefficient of 0.78 [see Fig. 11(a)]. This suggests that the continuous growth signal in IC2 represents long-term creep behavior influenced by rainfall, while the periodic deformation corresponds to slope movement driven by FRWL. In conclusion, the combined effect of FRWL and rainfall is the primary trigger of IC2 deformation at the toe of the Shuizhuyuan landslide.

Fig. 9 demonstrates that IC3 plays a critical role in controlling toe movement. Given that FRWL may induce not only periodic deformation but also stepwise deformation [4], [17], [38], a sigmoid function is employed to fit the time series of IC3 [refer to Fig. 11(b)]. The results show that the IC3s t-eigenvector exhibits step deformation characteristics, with an R^2 value of 0.992, a normally distributed fitting error, and an RMSE of 1.462. We observed that the acceleration of IC3 deformation corresponds to the RWL drop, although a delay exists between these variables. This delay may be attributed to the permeability coefficient being lower than the rate of RWL drop. Therefore, it can be inferred that the RWL drop serves as a trigger for inducing step deformation at the toe in Shuizhuyuan landslide site. We observed that the value of IC3 did not increase as expected during the period of rapid RWL decline in 2022–2024. Through consultation of local data, we found that, since 2022, relevant authorities have implemented emergency treatment measures for the Shuizhuyuan landslide. These effects may explain the reduction in IC3 step deformation.

Time lag is a critical parameter for understanding the response characteristics of landslide deformation. Fig. 10(a) and (b) illustrates the delayed phenomenon among the time series of independent components, cumulative rainfall, and FRWL. Specifically, the correlation between IC1 and cumulative rainfall peaks

after 77 days, while the correlation between IC2 and FRWL peaks after 71 days. This long-term delay may be associated with the low permeability of the sliding mass. Analysis of the IC2 component at the toe and the combined effects reveals that the correlation coefficient reaches its maximum at a delay time of 65 days. This indicates that these two driving factors accelerate the deformation response of the toe.

C. Fluid–Solid Coupling Analysis

The hydraulic diffusion coefficient is a critical parameter for describing a landslide's response to rainfall infiltration [23]. Many researchers estimate this coefficient by InSAR deformation time series and rainfall records using a 1-D pore water diffusion model [5], [12]. In the TGR area, the near-polar observation geometry of SAR is not sensitive to displacements in the north–south direction, leading to underestimation of deformation in many landslides. Nevertheless, this inversion method relies on the relationship between transient pore water pressure and the InSAR deformation time series for iterative optimization. As a result, the underestimation of InSAR deformation has a negligible impact on the accuracy of the parameter inversion. For instance, despite the north–south orientation of the Xinpu landslide in the TGR area, the method yields satisfactory results [12]. Prior to the fluid–solid coupling analysis, the effective pore water diffusion coefficient of the Shuizhuyuan landslide was determined using InSAR deformation time series controlled by rainfall at the landslide's trailing edge. In this study, a depth window of ± 1.0 m was applied to identify the optimal estimate, with the final solution corresponding to a residual error of less than 0.2%. The normalized deformation rate and pore water pressure are presented in Fig. 12, yielding a hydraulic diffusion coefficient of $1.22^{-0.03}_{+0.19} \times 10^{-5}$ m^2/s at a 95% confidence. This coefficient is reasonable for a deep sliding and slow-moving landslide and aligns closely with previous research findings from the TGR [12]. The empirical value C_0 proposed by Iverson was utilized as conversion constant between the hydraulic diffusion coefficient and permeability coefficient. As a result, the saturated permeability coefficient of the Shuizhuyuan landslide was determined to be 0.11 m/d, consistent with findings from the Jiuxianping and Shuping landslides in the TGR [17], [41]. These landslides share similar characteristics, being driven by hydrodynamic pressure.

The rainfall record for a hydrological year (Scenario 1) and the average rate of RWL rise and fall (Scenario 2) are utilized as calculation conditions for dynamic seepage analysis. Fig. 13(a)–(c) depicts the pore pressure contour of rainfall (365 days), RWL decline (0.2 m/d, 151 days), and RWL rise (0.5 m/d, 365 days).

It can be observed from Fig. 13(a) that rainfall infiltration results in transient saturation within the sliding mass, which increases its weight and the sliding force, causing displacement along the slope and reducing stability [21]. The potential failure mode of Shuizhuyuan landslide under rainfall conditions is assessed by coupling seepage analysis and strength reduction method, as depicted in Fig. 13(d). Although the InSAR results show rainfall-induced deformation primarily at the middle and trailing edge, numerical simulation indicates that failure may
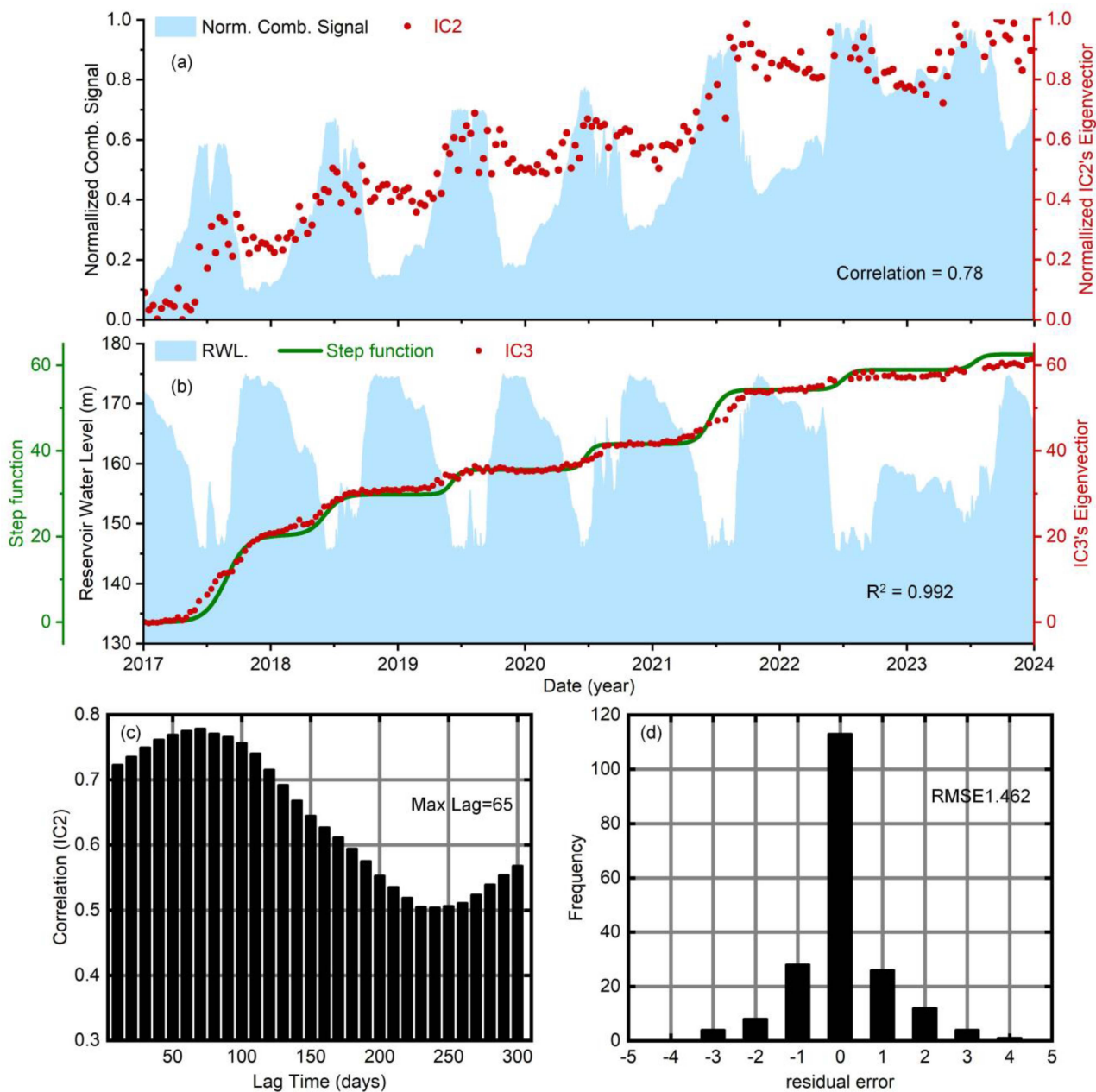
Fig. 11. (a) Comparison between IC2 (red dot) and the normalized combined signal (cyan areas) after combining the precipitation and RWL records. (b) Comparison between IC3 (red dot) and the simulate step function (green line). (c) Relationship between correlation of IC2 and lag time. (d) Fitting error distribution of IC3.

occur at the front of the landslide, exhibiting typical traction characteristic. Stability analysis shows an FOS of 1.74 under these conditions and shows a relatively stable security state.

Fig. 13(b) illustrates the pore pressure distribution resulting from a decrease in RWL at Shuizhuyuan landslide, from 175.0 to 145.0 m at a rate of 0.2 m/d (Scenario 2). Due to the relatively low permeability coefficient of sliding mass compared with the rate of RWL drop, groundwater within the slope cannot drain in time, leading to significant hydrodynamic pressure at the slope's front edge [indicated by the arrow in Fig. 13(b)]. This hydraulic gradient generates a substantial sliding force. Furthermore, the disappearance of hydrostatic pressure in the hydrofluctuation

belt significantly reduces slope stability, causing deformation at the toe. We coupled the results of seepage analysis and calculated the possible failure mode of Shuizhuyuan landslide under the condition of RWL drop (0.2 m/d) by strength reduction method, as shown in Fig. 13(e). This failure mode is similar to that under rainfall conditions, with large deformations occurring at the toe. Under these seepage conditions, the slope's FOS is 1.45, indicating that, compared with rainfall, the primary instability threat to the Shuizhuyuan landslide is driven by the RWL drop in the TGR.

To investigate the impact of rising RWL on the stability of the Shuizhuyuan landslide, the RWL was raised from 145.0 to
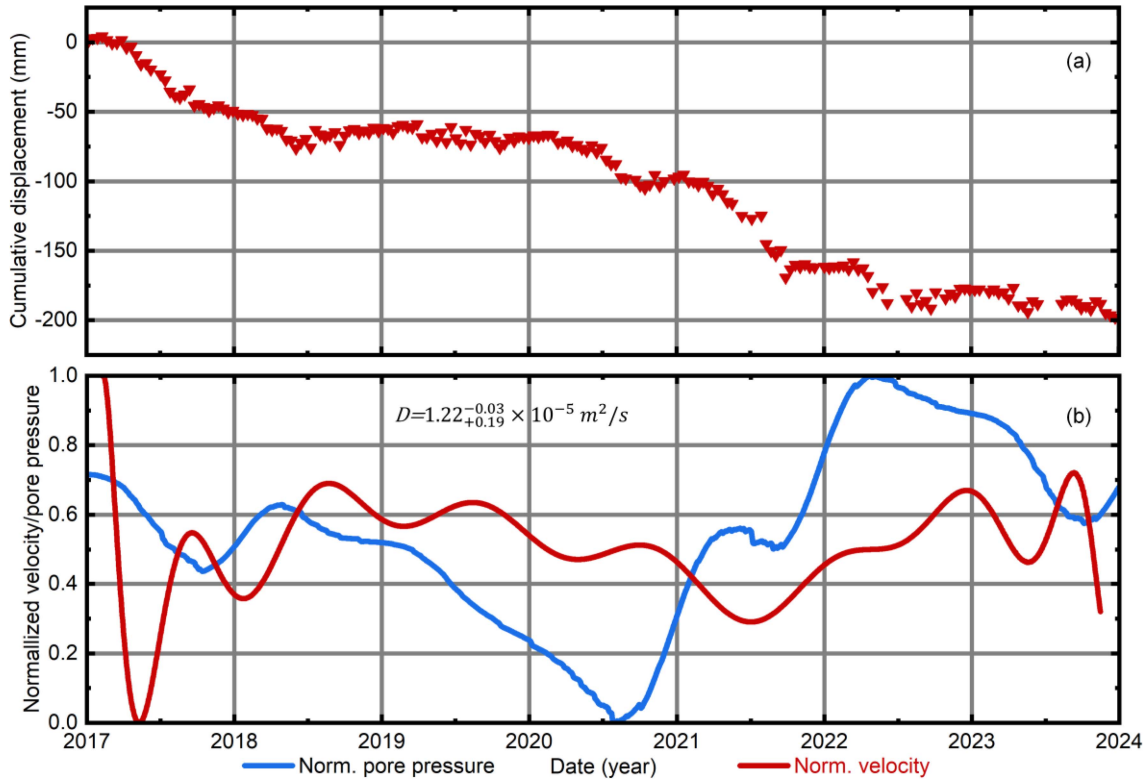
Fig. 12. (a) Cumulative displacement of the Shuizhuyuan landslide during 2017–2023. (b) Normalized velocity and the pore pressure derived by the 1-D diffusion model. D is the inferred hydraulic diffusivity.
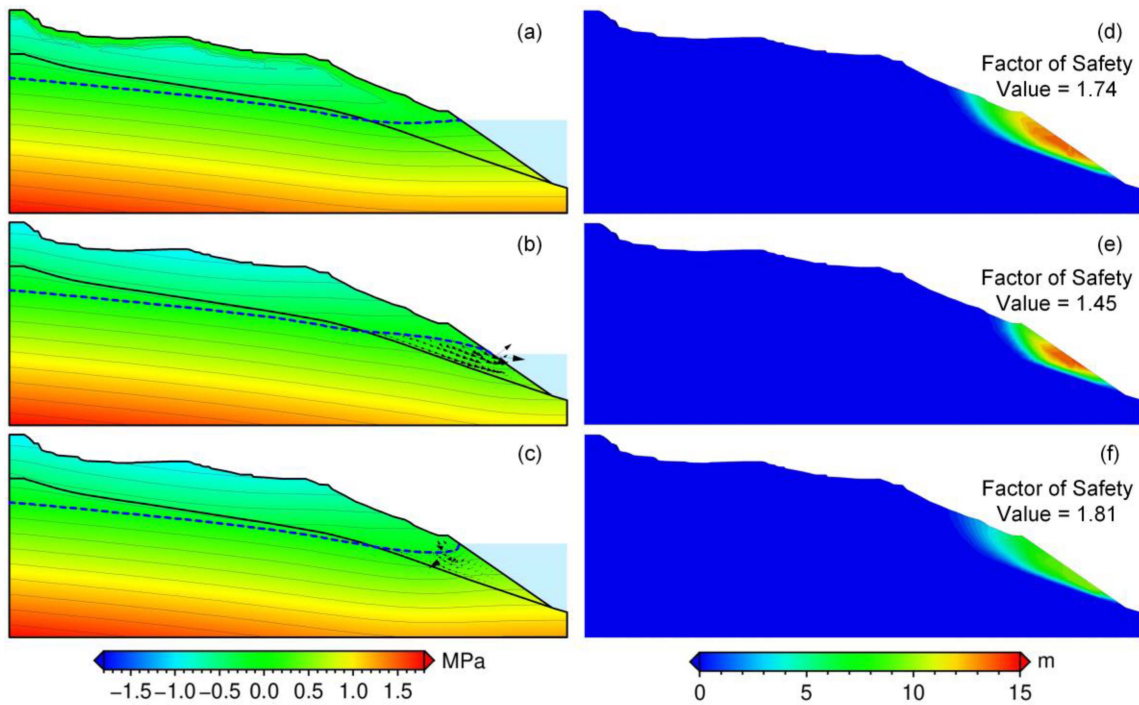

Fig. 13. (a) Seepage and stability assessment simulation results of scenario 1 and scenario 2. (a)–(c) Represent pore water pressure nephograms under the scenarios of rainfall, water-level decline, and water-level rise. (d)–(f) Represent displacement nephograms calculated by intensity reduction under the scenarios of rainfall, water-level decline, and water-level rise.
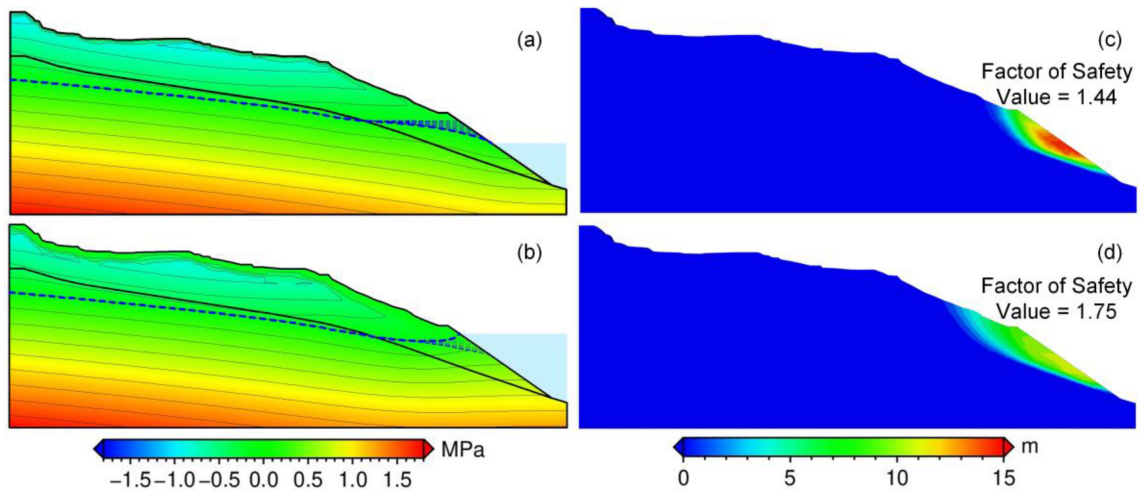
Fig. 14.   Seepage and stability assessment simulation results of scenario 3. The pore water pressure nephograms of (a) coupling rainfall and water-level decline and (b) coupling rainfall and water-level rise. (c) Displacement nephograms calculated by intensity reduction under scenarios of (c) coupling rainfall and water-level decline and (d) coupling rainfall and water-level rise.

175.0 m at a rate of 0.5 m/d in Scenario 2. Seepage analysis results revealed a hydraulic head difference between the surface and interior of the sliding mass [see Fig. 13(c)], attributed to a hydraulic gradient caused by the rapid rise in RWL exceeding the permeability coefficient. The seepage force from the exterior toward the interior, along with counterpressure from hydrostatic pressure, significantly enhanced antisliding forces within the landslide. Fluid–solid coupling analysis indicated that displacement remained concentrated at the front and toe of the landslide following increased RWL, demonstrating typical tractive characteristics. Compared with the displacement under RWL drop, the magnitude of deformation at the toe decreased significantly after the RWL rise, indicating elastic deformation due to FRWL. While displacement increased during the RWL drop, some rebounds occurred as antisliding forces were enhanced during the rise in RWL. The time vector of independent component IC2 further confirmed the presence of this elastic deformation. Stability results showed that, under these conditions, the FOS reached 1.81, suggesting that slope stability can be significantly improved by rising RWL.

V. DISCUSSION

A. Failure and Deformation Mode of Shuizhuyuan Landslide

Considering the potential influence of rainfall and FRWL on the deformation results of the toe detected by InSAR, it is crucial to accurately determine the possible failure deformation mode of Shuizhuyuan landslide. Therefore, numerical analysis incorporating two hydraulic boundary conditions (rainfall and FRWL) was conducted to perform stress analysis (Scenario 3). The seepage results, as presented in Fig. 14(a), indicate that, in addition to hydrodynamic pressure at the landslide front caused by RWL drop, significant hydraulic gradients also occur at the middle and trailing edge of the landslide due to rainfall infiltration. The FOS under the coupling condition is 1.44. Combined with the failure and deformation results, as presented in Fig. 14(c), it is evident that the impact of the

hydraulic gradient generated by rainfall on the stability of the front edge under the combined effect can be disregarded. In the seepage field coupled with rainfall and RWL rise [see Fig. 14(b)], the landslide is influenced simultaneously by seepage force, hydrostatic pressure from RWL, and hydrodynamic pressure from continuous rainfall. The FOS under this coupling condition is 1.75, and there is an increase in toe deformation compared with that caused by rising RWL, indicating that the influence of rainfall on landslide stability during rising RWL cannot be overlooked.

Based on the simulation results under the hydraulic conditions mentioned above, it is found that the potential failure of Shuizhuyuan landslide may occur at its front edge, where the sliding surface exhibits typical circular arc characteristics [see Figs. 13(d)–(f) and 14(c) and (d)]. The distribution of failure deformation shows that large deformations are concentrated at the toe, displaying the characteristics of traction progressive deformation. Analyzing both internal and external dynamic factors, the primary mechanism driving this deformation and instability is the hydrodynamic pressure caused by the TGR water-level drop. Therefore, we infer that the failure deformation of the Shuizhuyuan landslide follows a traction progressive deformation mode characterized by circular arc sliding surface traction, driven by seepage from RWL drop. This mode of deformation is commonly observed in landslides within the TGR area. In the prevention and treatment of the Shuizhuyuan landslide, particular attention should be paid to the rate of RWL drop in the TGR and the deformation of the toe.

B. Interpretation of Deformation Mechanism Based on Numerical Simulation Results

InSAR results reveal that the deformation exhibits complex temporal and spatial patterns. Numerical simulation is employed to elucidate the mechanical mechanism underlying these deformation features. During rainfall infiltration, the transient saturation of the soil increases the weight of the sliding mass,
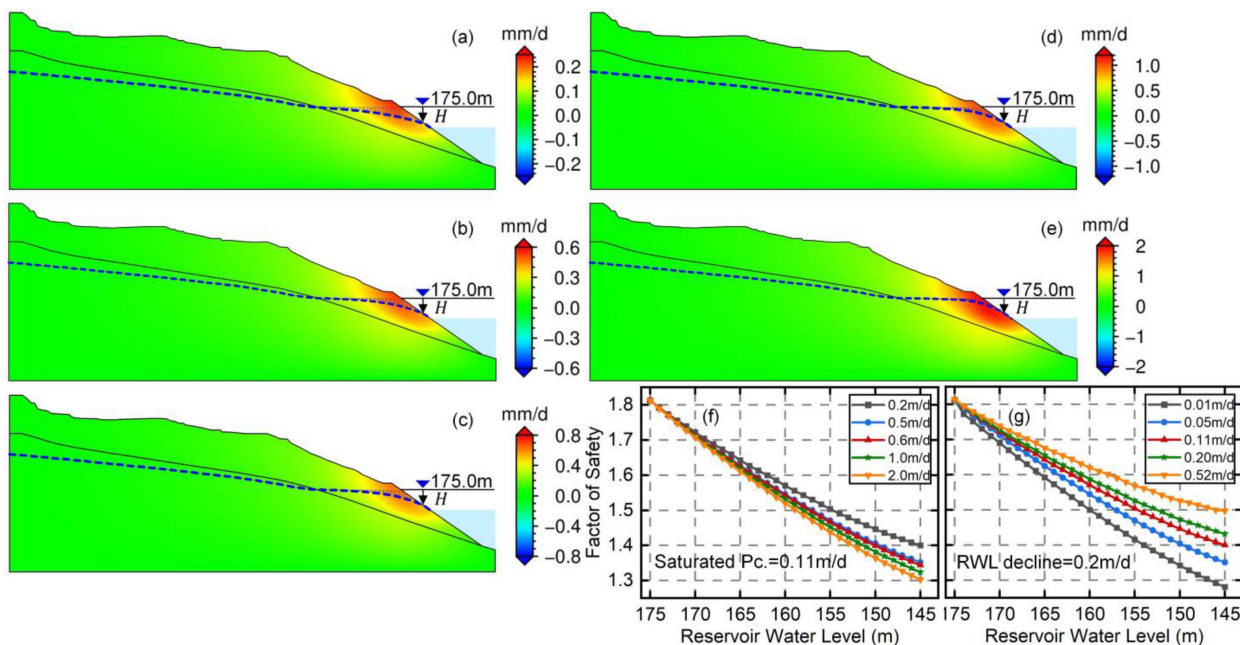
Fig. 15.   Displacement rate simulation results of scenario 4. (a) 0.2 mm/d. (b) 0.5 mm/d. (c) 0.6 mm/d. (d) 1.0 mm/d. (e) 2.0 mm/d. (f) Response characteristics of safety factor under different rates of water-level drop. The blue dashed line shows the phreatic line of groundwater. (g) Response characteristics of safety factor under different permeability coefficients.

creating favorable conditions for the sliding force to increase along the free surface. Simultaneously, the increase of pore pressure leads to the disappear of matrix suction in unsaturated soil and a reduction in effective stress, thereby decreasing the soil's shear strength. Steep slopes are particularly vulnerable to surface runoff, which significantly hinders rainfall infiltration. In contrast, gentler terrain (such as the toe or shoulder of a slope) accumulates a substantial amount of rainwater, resulting in stress concentration and pronounced hydraulic gradients [21], as shown in Fig. 13(a). Generally, the hydrodynamic pressure within the soil is positively correlated with the hydraulic gradient [25]. The combination of hydrodynamic pressure and sliding forces causes soil particles to slip in the direction of seepage. This explains the considerable displacement observed at the middle and trailing edges of landslides during rainfall events. Although InSAR detects significant deformation triggered by rainfall-induced landslides, stability analysis indicates that rainfall has a limited effect on the overall instability of the Shuizhuyuan landslide.

Cross-correlation analysis of InSAR results and stress analysis from fluid–solid coupling indicates that the primary factor driving deformation and instability at the slope toe is the drop in RWL. Since the permeability coefficient of the sliding mass is lower than the rate of RWL decline, a drop in RWL from 175.0 to 145.0 m causes a hysteresis in the groundwater saturation line. This line bulges toward the hydrofluctuation belt and overflows from the slope (as shown by the black arrow in Fig. 15), indicating that groundwater levels within the slope are significantly higher than the reservoir level. This induces hydrodynamic pressure from the interior to the exterior of the previously stable seepage channel, reducing landslide stability and causing slope deformation. Several studies have shown that

this hysteresis is closely related to the rate of RWL drop [25], [42], [43]. To assess the extent of its impact on displacement rates and landslide stability, five simulation conditions (Scenario 4) were designed [25], [43], [44]. The groundwater overflow elevation is represented by the height difference H from the overflow point of the saturation line to an RWL of 175.0 m. As shown in Fig. 15, a faster rate of RWL decline corresponds to a smaller H value, a higher groundwater overflow elevation, and increased hydrodynamic pressure. Simulation results demonstrate that the groundwater hysteresis significantly accelerates the displacement rate at the toe [see Fig. 15(a)–(e)]. Furthermore, stability results indicate a lower FOS for landslides. These findings provide evidence that hydrodynamic pressure, driven by the hydraulic head difference inside and outside the slope, is the primary mechanical mechanism responsible for the deformation of the Shuizhuyuan landslide during RWL drop.

Due to the significantly higher rate of RWL rise compared with the permeability coefficient of the sliding mass, a hysteresis effect occurs in the groundwater level at the toe as the RWL increases from 145.0 to 175.0 m. However, groundwater at the interface between the sliding mass and bedrock has not yet dissipated, causing the internal saturation line of the slope to exhibit a distinct upward bend. This difference in hydraulic head between the RWL and the sliding mass generates a seepage force from the exterior to the interior. In addition, the rising RWL reapplies hydrostatic pressure, exerting a counterpressure effect on the slope surface. These combined effects—seepage force and counterpressure—will enhance the stability of hydrodynamic pressure landslides [25], explaining the significant increase in the FOS and the reduction of large deformation at the toe in the numerical simulations [see Fig. 15(f)]. Displacement time-series results (IC2) at the toe indicate cyclic recovery of deformation
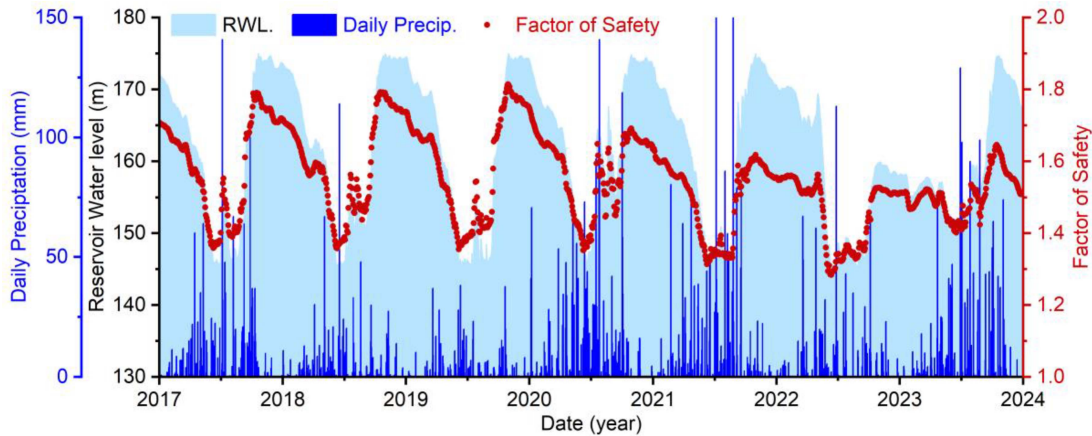
Fig. 16.   Dynamic response characteristics of FOS.

during RWL rise. However, as shown in Fig. 10(b), the cyclic deformation signal at the landslide front is superimposed on a continuous upward trend, suggesting that deformation induced by FRWL contains both elastic and plastic components. Elastic deformation corresponds to periodic changes in effective stress caused by FRWL, while the reduction in shear strength at the toe leads to irreversible plastic deformation. Overall, the seepage force generated by rising RWL and the counterpressure effect of hydrostatic pressure are identified as the primary mechanical mechanisms driving the periodic deformation of the Shuizhuyuan landslide.

Fig. 15(a)–(f) illustrates that the hysteresis of the groundwater saturation line during the RWL decline reduces slope stability and induces deformation at the toe. InSAR observations also detected a time delay in step deformation triggered by the RWL drop. These hysteresis and delay occur because the landslide's permeability coefficient is lower than the rate of RWL decline [25]. The greater the disparity between these two factors, the more rapidly stability decreases. To this end, we designed five different permeability coefficients to discuss the stability change on RWL decline. Typically, the permeability coefficient of a mixture of gravel and silty clay does not exceed that of silty sand, with a lower empirical limit of 6.0×10^{-4} cm/s (0.518 m/d). In addition, the permeability coefficient of this accumulated deposit is generally higher than 0.01 m/d. Therefore, we selected five permeability coefficients for analysis: 0.01, 0.05, 0.11, 0.2, and 0.52 m/d. Fig. 15(g) shows the stability change of landslide with different permeability coefficients under the same rate of FRWL (scenario 2). The results indicate that a lower permeability coefficient leads to a faster stability response to FRWL. At an RWL of 145.0 m, the FOS is lower with low permeability, suggesting a higher risk of failure. It can be seen that the hydraulic effects of the reservoir play a critical role in influencing landslide deformation and stability.

C. Response Rule of Landslide FOS

The FOS in Scenario 3 reveals the dynamic response of Shuizhuyuan landslide stability during the InSAR observation period. The results show that the response of FOS is strongly correlated with FRWL, exhibiting typical periodic characteristics. The FOS decreases rapidly when the RWL drops and increases synchronously as the RWL rises. This response pattern is consistent with previous research on hydrodynamic pressure landslides in the TGR area [17]. We observed that heavy rainfall, as depicted in Fig. 16, did not significantly reduce the FOS, indicating that the rainfall has a limited impact on Shuizhuyuan landslide stability. Notably, there is a slight overall declining trend in the FOS, and the simulation results of displacement also suggest the potential for plastic deformation. Given that FRWL may cause erosion and further strain softening along the reservoir bank [27], the risk of landslide instability during periods of RWL drop should not be overlooked. InSAR technology, as an advanced method for observing Earth, can be employed to enhance deformation monitoring and time-series analysis during FRWL, as well as aid in assessing the risk of the Shuizhuyuan landslide.

VI. CONCLUSION

In this study, InSAR technology and numerical simulation methods were utilized to comprehensively analyze the spatiotemporal deformation patterns, potential failure modes, deformation mechanisms, and dynamic response characteristics of the FOS of the Shuizhuyuan landslide.

InSAR analysis detected significant deformation at the front, middle, and trailing edges of the Shuizhuyuan landslide, with a maximum rate of −60 mm/yr. Using the ICA method, three deformation components related to the landslide movement were identified. These components are spatially concentrated at the landslide's trailing edge, toe, and front, and temporally exhibit the characteristics of continuous increase, periodicity, and stepwise deformation, respectively. Cross-correlation analysis of the spatial and temporal patterns of these independent components revealed that IC1 is predominantly controlled by rainfall, IC2 is influenced by the combined effects of FRWL and rainfall, and IC3s stepwise deformation is driven by RWL decline. Overall, the correlation analysis of the InSAR-derived deformation results provides geometric insights into the complex deformation mechanisms governing the Shuizhuyuan landslide.

The saturation permeability coefficient of the sliding mass in seepage analysis is modified by InSAR deformation. Fluid–solid coupling simulations confirmed that the Shuizhuyuan landslide undergoes traction progressive failure along a circular arc sliding surface due to seepage, primarily driven by RWL drop. The hydrodynamic pressure caused by rainfall infiltration and the sliding force resulting from increasing soil weight are the driving factors of deformation at the middle and trailing edge of the landslide. Groundwater hysteresis, resulting from the drop in RWL, is the primary mechanical mechanism driving deformation at the toe. Conversely, the seepage force from rising RWL and the counterpressure effect of hydrostatic pressure contribute to elastic deformation. The FOS fluctuates in synchronization with the TGR water level, exhibiting typical periodic feature. While rainfall has a limited effect on the safety factor, a slight overall decline in FOS was observed, indicating potential long-term impacts that warrant attention.

In summary, this study investigates the deformation of the Shuizhuyuan landslide from a new perspective by combining InSAR spatiotemporal deformation patterns and numerical simulation of the stress–strain state. This relevant investigation provides a feasible auxiliary means for preventing and assessing the safety of reservoir landslide disasters in the future.

REFERENCES

[1] F. Wang, Y. M. Zhang, Z. T. Huo, X. M. Peng, S. M. Wang, and S. Yamasaki, "Mechanism for the rapid motion of the Qianjiangping landslide during reactivation by the first impoundment of the Three Gorges Dam reservoir, China," *Landslides*, vol. 5, no. 4, pp. 379–386, Nov. 2008, doi: 10.1007/s10346-008-0130-7.

[2] C. Zhou, Y. Cao, K. L. Yin, E. Intrieri, F. Catani, and L. X. Wu, "Characteristic comparison of seepage-driven and buoyancy-driven landslides in Three Gorges Reservoir area, China," *Eng. Geol.*, vol. 301, May 2022, Art. no. 106590, doi: 10.1016/j.enggeo.2022.106590.

[3] C. Zhao, Y. Kang, Q. Zhang, Z. Lu, and B. Li, "Landslide identification and monitoring along the Jinsha River catchment (Wudongde Reservoir area), China, using the InSAR method," *Remote Sens.*, vol. 10, no. 7, Jul. 2018, Art. no. 993, doi: 10.3390/rs10070993.

[4] B. Han, B. Tong, J. K. Yan, C. R. Yin, L. Chen, and D. Y. Li, "The monitoring-based analysis on deformation-controlling factors and slope stability of reservoir landslide: Hongyanzi landslide in the South-West of China," *Geofluids*, vol. 2018, no. 1, 2018, Art. no. 7391517, doi: 10.1155/2018/7391517.

[5] X. Shi et al., "Hydrological control shift from river level to rainfall in the reactivated Guobu slope besides the Laxiwa hydropower station in China," *Remote Sens. Environ.*, vol. 265, Nov. 2021, Art. no. 112664, doi: 10.1016/j.rse.2021.112664.

[6] K. R. Dai et al., "Dynamic landslides susceptibility evaluation in Baihetan Dam area during extensive impoundment by integrating geological model and InSAR observations," *Int. J. Appl. Earth Observ. Geoinf.*, vol. 116, Feb. 2023, Art. no. 103157, doi: 10.1016/j.jag.2022.103157.

[7] L. L. Xiao, J. J. Wang, S. Ward, and L. X. Chen, "Numerical modeling of the June 24, 2015, Hongyanzi landslide generated impulse waves in Three Gorges Reservoir, China," *Landslides*, vol. 15, no. 12, pp. 2385–2398, Dec. 2018, doi: 10.1007/s10346-018-1057-2.

[8] X. Xiong, Z. M. Shi, Y. L. Xiong, M. Peng, X. L. Ma, and F. Zhang, "Unsaturated slope stability around the Three Gorges Reservoir under various combinations of rainfall and water level fluctuation," *Eng. Geol.*, vol. 261, Nov. 2019, Art. no. 105231, doi: 10.1016/j.enggeo.2019.105231.

[9] W. A. Zhang, X. Y. Meng, L. Q. Wang, and F. S. Meng, "Stability analysis of the reservoir bank landslide with weak interlayer considering the influence of multiple factors," *Geomatics Natural Hazards Risk*, vol. 13, no. 1, pp. 2911–2924, Dec. 2022, doi: 10.1080/19475705.2022.2149356.

[10] S. L. Xu and R. Q. Niu, "Displacement prediction of Baijiabao landslide based on empirical mode decomposition and long short-term memory neural network in Three Gorges area, China," *Comput. Geosci.*, vol. 111, pp. 87–96, Feb. 2018, doi: 10.1016/j.cageo.2017.10.013.

[11] J. H. Dong, R. Q. Niu, B. Q. Li, H. Xu, and S. Y. Wang, "Potential landslides identification based on temporal and spatial filtering of SBAS-InSAR results," *Geomatics Natural Hazards Risk*, vol. 14, no. 1, pp. 52–75, Dec. 2023, doi: 10.1080/19475705.2022.2154574.

[12] W. J. Zheng et al., "Enhanced kinematic inversion of 3-D displacements, geometry, and hydraulic properties of a north-south slow-moving landslide in Three Gorges Reservoir," *J. Geophys. Res.-Solid Earth*, vol. 128, no. 6, Jun. 2023, Art. no. e2022JB026232, doi: 10.1029/2022jb026232.

[13] J. Du et al., "InSAR-based active landslide detection and characterization along the upper reaches of the yellow river," *IEEE J. Sel. Topics Appl. Earth Observ. Remote Sens.*, vol. 16, pp. 3819–3830, Mar. 2023, doi: 10.1109/jstars.2023.3263003.

[14] A. Guo, Q. Sun, J. Hu, W. Zheng, R. Gui, and Y. Yu, "MUSEnet: High temporal-frequency estimation of landslide deformation field through joint InSAR and hydrological observations using deep learning," *IEEE J. Sel. Topics Appl. Earth Observ. Remote Sens.*, vol. 17, pp. 1485–1499, 2024, doi: 10.1109/jstars.2023.3338449.

[15] W. Zheng et al., "Enhancing 4-D landslide monitoring and block interaction analysis with a novel Kalman-filter-based InSAR approach," *J. Geophys. Res.-Earth Surf.*, vol. 129, no. 11, Nov. 2024, Art. no. e2024JF007923, doi: 10.1029/2024jf007923.

[16] W. Zheng et al., "Investigating kinematics and triggers of slow-moving reservoir landslide using an improved MT-InSAR method," *Geomatics Natural Hazards Risk*, vol. 14, no. 1, Dec. 2023, Art. no. 2289835, doi: 10.1080/19475705.2023.2289835.

[17] Z. H. Fan, S. M. Wang, L. Wang, F. Guo, F. Y. Nan, and Y. X. Hu, "Emergency treatment effect evaluation of rear-slope cutting and front-slope pressing on a hydrodynamic pressure landslide: A case study of the Shuping landslide in the Three Gorges Reservoir area," *Bull. Eng. Geol. Environ.*, vol. 83, no. 1, Jan. 2024, Art. no. 38, doi: 10.1007/s10064-023-03539-z.

[18] W. S. Sillers and D. G. Fredlund, "Statistical assessment of soil-water characteristic curve models for geotechnical engineering," *Can. Geotech. J.*, vol. 38, no. 6, pp. 1297–1313, Dec. 2001, doi: 10.1139/cgj-38-6-1297.

[19] T. S. Nguyen and S. Likitlersuang, "Reliability analysis of unsaturated soil slope stability under infiltration considering hydraulic and shear strength parameters," *Bull. Eng. Geol. Environ.*, vol. 78, no. 8, pp. 5727–5743, Dec. 2019, doi: 10.1007/s10064-019-01513-2.

[20] D. G. Fredlund and H. Rahardjo, *Soil Mechanics for Unsaturated Soils*. Hoboken, NJ, USA: Wiley, 1993.

[21] Z. H. Fan, S. M. Wang, L. Wang, F. Guo, J. J. Huang, and X. W. Li, "Deformation characteristics, mechanisms, and dominant factors involved in rainfall-hydrodynamic pressure landslides: A case study," *Environ. Earth Sci.*, vol. 82, no. 24, Dec. 2023, Art. no. 607, doi: 10.1007/s12665-023-11303-5.

[22] Y. Zhang, Z. Zhang, S. Xue, R. Wang, and M. Xiao, "Stability analysis of a typical landslide mass in the three gorges reservoir under varying reservoir water levels," *Environ. Earth Sci.*, vol. 79, no. 1, Jan. 2020, Art. no. 42, doi: 10.1007/s12665-019-8779-x.

[23] R. M. Iverson, "Landslide triggering by rain infiltration," *Water Resour. Res.*, vol. 36, no. 7, pp. 1897–1910, Jul. 2000, doi: 10.1029/2000wr900090.

[24] D. M. Gu, D. Huang, W. D. Yang, J. L. Zhu, and G. Y. Fu, "Understanding the triggering mechanism and possible kinematic evolution of a reactivated landslide in the Three Gorges Reservoir," *Landslides*, vol. 14, no. 6, pp. 2073–2087, Dec. 2017, doi: 10.1007/s10346-017-0845-4.

[25] M. G. Tang et al., "Activity law and hydraulics mechanism of landslides with different sliding surface and permeability in the Three Gorges Reservoir area, China," *Eng. Geol.*, vol. 260, Oct. 2019, Art. no. 105212, doi: 10.1016/j.enggeo.2019.105212.

[26] C. H. Wang and W. Guo, "Prediction of landslide displacement based on the variational mode decomposition and GWO-SVR model," *Sustainability*, vol. 15, no. 6, Mar. 2023, Art. no. 5470, doi: 10.3390/su15065470.

[27] X. Hu, H. Tang, C. Li, and R. Sun, "Stability of Huangtupo riverside slumping mass II# under water level fluctuation of Three Gorges Reservoir," *J. Earth Sci.*, vol. 23, no. 3, pp. 326–334, Jun. 2012, doi: 10.1007/s12583-012-0259-0.

[28] C. H. Wang, G. C. Lin, W. Guo, Q. J. Meng, K. Yang, and J. Y. Ji, "Landslide displacement prediction based on CEEMDAN and grey wolf optimized-support vector regression model," *Front. Earth Sci.*, vol. 10, Aug. 2022, Art. no. 961528, doi: 10.3389/feart.2022.961528.

[29] W. Guo, Q. J. Meng, X. Wang, Z. T. Zhang, K. Yang, and C. H. Wang, "Landslide displacement prediction based on variational mode decomposition and GA-Elman model," *Appl. Sci.*, vol. 13, no. 1, Jan. 2023, Art. no. 450, doi: 10.3390/app13010450.

[30] L. Zhang, X. L. Ding, and Z. Lu, "Ground settlement monitoring based on temporarily coherent points between two SAR acquisitions," *ISPRS-J. Photogramm. Remote Sens.*, vol. 66, no. 1, pp. 146–152, Jan. 2011, doi: 10.1016/j.isprsjprs.2010.10.004.

[31] L. Zhang, X. Ding, and Z. Lu, "Modeling PSInSAR time series without phase unwrapping," *IEEE Trans. Geosci. Remote Sens.*, vol. 49, no. 1, pp. 547–556, Jan. 2011, doi: 10.1109/tgrs.2010.2052625.

[32] Z. W. Li, X. L. Ding, C. Huang, G. Wadge, and D. W. Zheng, "Modeling of atmospheric effects on InSAR measurements by incorporating terrain elevation information," *J. Atmos. Sol.-Terr. Phys.*, vol. 68, no. 11, pp. 1189–1194, Jul. 2006, doi: 10.1016/j.jastp.2006.03.002.

[33] J. Cohen-Waeber, R. Bürgmann, E. Chaussard, C. Giannico, and A. Ferretti, "Spatiotemporal patterns of precipitation-modulated landslide deformation from independent component analysis of InSAR time series," *Geophys. Res. Lett.*, vol. 45, no. 4, pp. 1878–1887, Feb. 2018, doi: 10.1002/2017gl075950.

[34] R. Tomás, Z. Li, J. Lopez-Sanchez, P. Liu, and A. Singleton, "Using wavelet tools to analyse seasonal variations from InSAR time-series data: A case study of the Huangtupo landslide," *Landslides*, vol. 13, no. 3, pp. 437–450, Jun. 2016, doi: 10.1007/s10346-015-0589-y.

[35] N. Lu, B. Sener-Kaya, A. Wayllace, and J. W. Godt, "Analysis of rainfall-induced slope instability using a field of local factor of safety," *Water Resour. Res.*, vol. 48, Sep. 2012, Art. no. W09524, doi: 10.1029/2012wr011830.

[36] N. L. Wen et al., "Periodic displacement accurate extraction of reservoir active slopes through InSAR observation and independent component analysis-based wavelet transform," *Int. J. Appl. Earth Observ. Geoinf.*, vol. 130, Jun. 2024, Art. no. 103919, doi: 10.1016/j.jag.2024.103919.

[37] K. Zhu, X. Zhang, Q. Sun, H. Wang, and J. Hu, "Characterizing spatiotemporal patterns of land deformation in the Santa Ana Basin, Los Angeles, from InSAR time series and independent component analysis," *Remote Sens.*, vol. 14, no. 11, Jun. 2022, Art. no. 2624, doi: 10.3390/rs14112624.

[38] H. Q. Yang, K. L. Song, L. C. Chen, and L. L. Qu, "Hysteresis effect and seasonal step-like creep deformation of the Jiuxianping landslide in the Three Gorges Reservoir region," *Eng. Geol.*, vol. 317, May 2023, Art. no. 107089, doi: 10.1016/j.enggeo.2023.107089.

[39] X. H. Huang, F. Guo, M. L. Deng, W. Yi, and H. F. Huang, "Understanding the deformation mechanism and threshold reservoir level of the floating weight-reducing landslide in the Three Gorges Reservoir area, China," *Landslides*, vol. 17, no. 12, pp. 2879–2894, Dec. 2020, doi: 10.1007/s10346-020-01435-1.

[40] H. M. Han, B. Shi, and L. Zhang, "Prediction of landslide sharp increase displacement by SVM with considering hysteresis of groundwater change," *Eng. Geol.*, vol. 280, Jan. 2021, Art. no. 105876, doi: 10.1016/j.enggeo.2020.105876.

[41] W. H. Xu et al., "Combining numerical simulation and deep learning for landslide displacement prediction: An attempt to expand the deep learning dataset," *Sustainability*, vol. 14, no. 11, Jun. 2022, Art. no. 6908, doi: 10.3390/su14116908.

[42] M. M. Berilgen, "Investigation of stability of slopes under drawdown conditions," *Comput. Geotech.*, vol. 34, no. 2, pp. 81–91, 2007, doi: 10.1016/j.compgeo.2006.10.004.

[43] F. M. Huang, X. Y. Luo, and W. P. Liu, "Stability analysis of hydrodynamic pressure landslides with different permeability coefficients affected by reservoir water level fluctuations and rainstorms," *Water*, vol. 9, no. 7, Jul. 2017, Art. no. 450, doi: 10.3390/w9070450.

[44] G. H. Sun, Y. T. Yang, W. Jiang, and H. Zheng, "Effects of an increase in reservoir drawdown rate on bank slope stability: A case study at the Three Gorges Reservoir, China," *Eng. Geol.*, vol. 221, pp. 61–69, Apr. 2017, doi: 10.1016/j.enggeo.2017.02.018.

Guoshi Liu received the M.Eng. degree in geodesy from Chang'an University, Xi'an, China, in 2014. He is currently working toward the Doctoral degree in surveying engineering with Central South University, Changsha, China.

From 2014 to 2024, he was a Lecturer with Shaoyang University, Shaoyang, China. His research interests focus on InSAR deformation monitoring and the stability evaluation of reservoir landslide.

Bin Wang received the M.Eng. degree in photogrammetry and remote sensing from Tongji University, Shanghai, China, in 2011.

His research interests include geological hazard monitoring and interpretation based on radar satellite remote sensing.

Qian Sun received the M.Eng. and Ph.D. degrees in geodesy and surveying engineering from Central South University, Changsha, China, in 2008 and 2015, respectively.

She is currently an Associate Professor with the School of Geographical Sciences, College of Geographic Science, Hunan Normal University, Changsha, China. Her research interests include geological hazard monitoring and interpretation based on radar satellite remote sensing.

Jun Hu (Senior Member, IEEE) received the M.Eng. and Ph.D. degrees in geodesy and surveying engineering from Central South University, Changsha, China, in 2008 and 2013, respectively.

From 2013 to 2014, he was a Postdoctoral Fellow with the Department of Land Surveying and Geo-Informatics, The Hong Kong Polytechnic University, Hong Kong. He is currently a Full Professor with the Department of Geomatics and Remote Sensing, School of Geosciences and Info-Physics, Central South University. He is the author of more than 60 papers in international peer-reviewed journals. His research interests include mapping multidimensional and high-precision deformations under complicated environment and its applications in geophysical fields.

Lei-Lei Liu received the Ph.D. degree in geotechnical engineering from The Hong Kong Polytechnic University, Hong Kong, in 2018.

He is currently an Associate Professor with the Department of Geological Engineering, Central South University, Changsha, China. His research interests include landslide monitoring and risk assessment, slope stability and reliability analysis, geotechnical uncertainty analysis, and slope large deformation analysis.

Wanji Zheng received the M.Eng. and Ph.D. degrees in geodesy from Central South University, Changsha, China, in 2018 and 2024, respectively.

His research interests include interferometric synthetic aperture radar and its applications on multidimensional landslide movement mapping.

Liye Zou was born in Changde, Hunan, China, in 2003. She is currently working toward the B.S. degree in surveying engineering with Shaoyang University, Shaoyang, China.

Her research interests focus on InSAR deformation monitoring and the stability evaluation of reservoir landslide.